Association between erythrocyte dynamics and vessel remodelling in developmental vascular networks

Qi Zhou[1], Tijana Perovic[2,+], Ines Fechner[2,+], Lowell T. Edgar[3], Peter R. Hoskins[4], Holger Gerhardt[2,5,6,7], Timm Krüger[1,*], and Miguel O. Bernabeu[3,*]

[1]School of Engineering, Institute for Multiscale Thermofluids, The University of Edinburgh, Edinburgh, UK
[2]Max-Delbrück-Center for Molecular Medicine in the Helmholtz Association (MDC), Berlin, Germany
[3]Centre for Medical Informatics, Usher Institute, The University of Edinburgh, Edinburgh, UK
[4]Centre for Cardiovascular Science, The University of Edinburgh, Edinburgh, UK
[5]Vascular Patterning Laboratory, Department of Oncology and Leuven Cancer Institute (LKI), KU Leuven, Belgium
[6]DZHK (German Center for Cardiovascular Research), Germany
[7]Berlin Institute of Health, Germany
[+]Equally contributing authors.
[*]Corresponding authors: timm.krueger@ed.ac.uk; miguel.bernabeu@ed.ac.uk

May 20th, 2020

Abstract

Sprouting angiogenesis is an essential vascularisation mechanism and consists of two phases: sprouting and remodelling. The remodelling phase is driven by rearrangements of endothelial cells (ECs) within the primitive vascular plexus. Prior work has uncovered how ECs polarise and migrate in response to flow-induced wall shear stress (WSS). However, the question of how the presence of red blood cells (RBCs), and their profound impact on microvascular haemodynamics, affect vascular remodelling has not been addressed. Here, we extend our computational framework to model blood flow in developmental mouse retina as a suspension of RBCs. Our results demonstrate a previously unreported highly heterogeneous distribution of RBCs in the post-sprouting vascular network. Furthermore, we report a strong association between vessel regression and RBC depletion, and identify plasma skimming as the driving mechanism. Live imaging in a developmental zebrafish model confirms this association. Taken together, our results indicate that RBC dynamics are fundamental for establishing the regional WSS differences driving vascular remodelling *via* their ability to modulate effective viscosity.

1 Introduction

Sprouting angiogenesis is an essential vascularisation mechanism and consists of two well-differentiated phases: sprouting and remodelling (Carmeliet, 2000; Potente et al., 2011). During the sprouting phase, a primitive network of vessels is laid out in response to proangiogenic factors *via* a well-established programme of cellular and molecular events (see Stapor et al., 2014 for a review). The remodelling phase is responsible for overhauling this primitive network into a hierarchical structure that can efficiently implement the transport capabilities of the cardiovascular system. During the remodelling phase, extensive vessel pruning is achieved primarily *via* dynamic rearrangement of endothelial cells (ECs) (Franco et al., 2015).

The mechanobiological regulation of ECs has been extensively studied, and it is known that ECs respond to their haemodynamic environment (Li et al., 2005). Studies in various animal models have shown that blood flow provides mechanical cues to drive vascular remodelling (*e.g.* chick embryo (Noble et al., 2004), mouse yolk sac (Lucitti et al., 2007), mouse aortic arch (Yashiro et al., 2007), zebrafish embryo (Bussmann et al., 2011; Chen et al., 2012; Kochhan et al., 2013; Franco et al., 2015) and mouse retina (Franco et al., 2015)). Furthermore, these studies have uncovered multiple molecular regulators of EC response to blood shear stress, such as VEGF (Baeyens et al., 2015), Wnt (Franco et al., 2016), Notch (Fang et al., 2017; Mack et al., 2017), TGFβ/BMP (Corti et al., 2011; Vion et al., 2018; Neal et al., 2019), DACH1 (Chang et al., 2017) and KLF2 (Doddaballapur et al., 2015).

In previous works, we demonstrated that blood shear stress coordinates EC migratory behaviour to achieve vessel regression during the remodelling phase (Franco et al., 2015, 2016; Vion et al., 2018). In particular, differences in wall shear stress (WSS) between neighbouring vessel segments lead to polarisation and migration of ECs away from vessel segments experiencing low WSS. In these studies, WSS was calculated using a mathematical flow model that assumes generalised Newtonian rheology (*i.e.* a homogeneous fluid of variable viscosity) without considering the presence of individual red blood cells

(RBCs). However, recent computational studies in microscale vessels have demonstrated that RBCs leave transient WSS luminal footprints and therefore could non-trivially modify the local WSS differences driving vascular remodelling (Freund and Vermot, 2014; Oulaid and Zhang, 2015; Hogan et al., 2019). This effect of RBCs is closely related to their crucial role in the formation of cell-free layer and the regulation of effective viscosity in microvascular blood flow (Obrist et al., 2010; Katanov et al., 2015; Lanotte et al., 2016; Balogh and Bagchi, 2018, 2019).

In the current study, we propose that the cellular nature of blood (primarily a suspension of RBCs) plays a key role establishing the local WSS differences driving vascular remodelling. We approach the problem computationally based on the mouse retina model of angiogenesis and provide validation in a developmental zebrafish model. We present simulations of cellular blood flow in vascular networks undergoing remodelling and characterise the bulk flow and RBC dynamics in them. Remarkably, we uncover a previously unreported heterogeneity in RBC perfusion throughout the developing network and a strong association between RBC depletion and vessel regression, which we further confirm experimentally in our zebrafish model *via* live imaging. In addition, our experiments confirm previous findings that the presence of RBCs is necessary for effective remodelling at a whole plexus level (Lucitti et al., 2007). Finally, we demonstrate that RBC depletion is primarily driven by the plasma skimming effect, *i.e.* the uneven distribution of RBC volume fraction at microvascular bifurcations (Krogh, 1921; Fenton et al., 1985), but uncover important deviations from existing theory caused by asymmetry in the cross-sectional distribution of haematocrit in vessels.

In line with our previous findings, we argue that RBC depletion constitutes a mechanism for the enhancement of the local WSS differences driving vascular remodelling. This is due to the direct relationship between RBC volume fraction, effective viscosity, and WSS. Additionally, we speculate that vascular remodelling driven by the principle of removing RBC-poor vessels from the primitive vasculature will lead to a network layout that avoids portions of the tissue being vascularised but with poorly oxygenated blood. This RBC-driven process, which is highly dynamical and emergent in nature, can importantly contribute to the optimal patterning of vascular networks during development.

2 Results

2.1 Simulation of cellular blood flow in microvascular network: validation versus experimental measurements

The vascular plexus of a wild-type mouse retina at postnatal day 5 (P5) was imaged and binarised following staining for collagen IV matrix sleeves (Col.IV) and ICAM2 luminal reporter (see protocol in Sec. 5.1.1). The ICAM2 mask delineates the perfused vessels in the network while the pixel-wise difference between the Col.IV and ICAM2 masks highlights vessel segments undergoing remodelling (Figure 1a) as demonstrated in Franco *et al.* (Franco et al., 2015). Therefore, the Col.IV mask constitutes a good approximation of the network morphology prior to these remodelling events. Indeed, the network recapitulates the log-normal distribution of vessel diameters previously reported by Bernabeu *et al.* (Bernabeu et al., 2014), with a maximum value of 45 μm and a mean of of 11.85

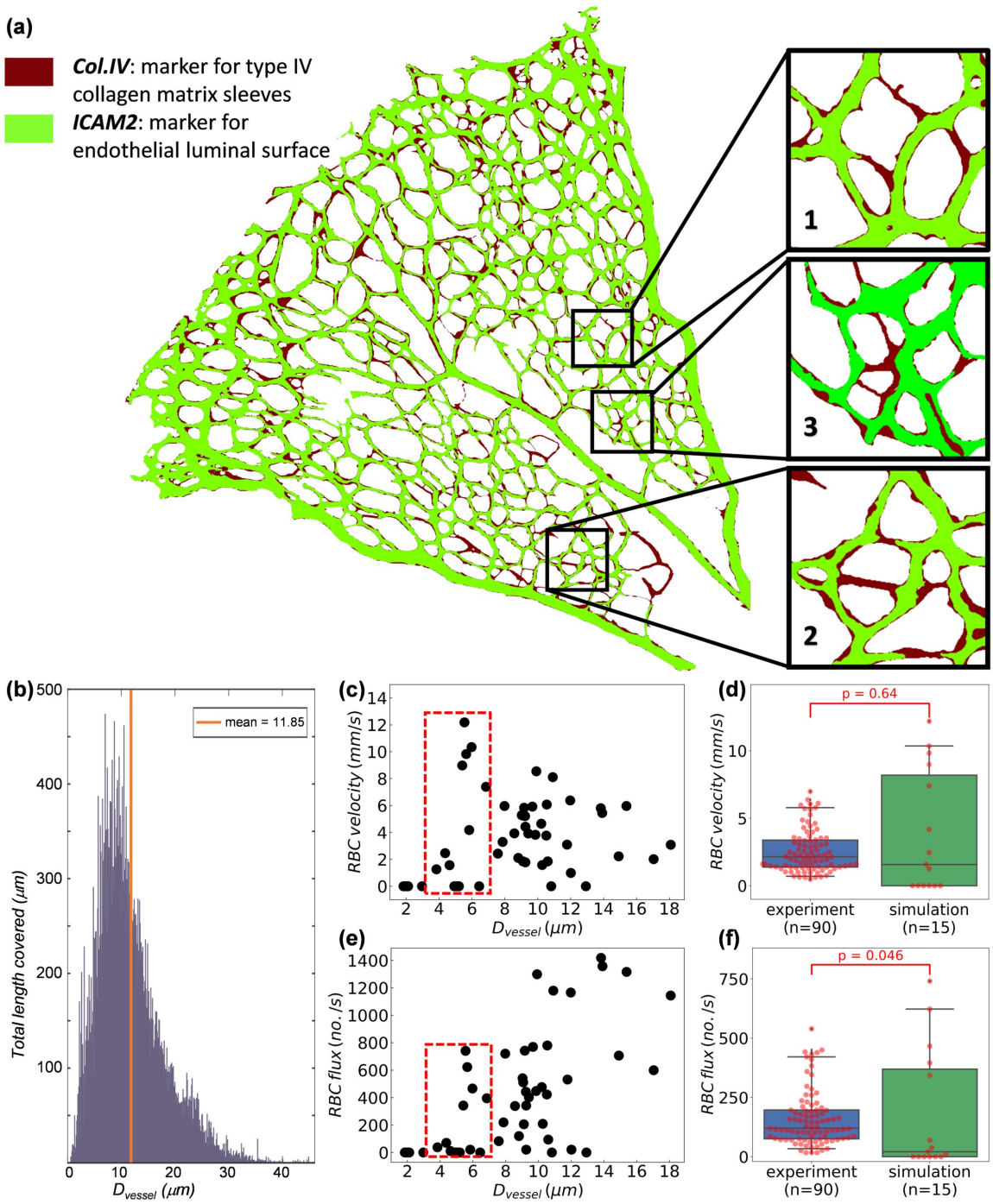

Figure 1: (a) A vascular plexus of postnatal day 5 (P5) mouse retina, with vessel lumina and collagen matrix sleeves labelled by ICAM2 (green) and Col.IV (dark red), respectively. The insets show three regions of interest (ROIs). (b) Network diameter histogram showing the total length covered by vessel segments of certain diameters. (c) Simulated RBC velocities and (e) RBC fluxes measured in divergent bifurcations within the ROIs. The box of red dashed lines in (c,e) highlight results from small vessels within diameter between 3 and 7 μm. (d,f) Comparison (Mann-Whitney U test) of simulated RBC velocities and RBC fluxes against *in vivo* measurements (Joseph et al., 2019; Guevara-Torres et al., 2016) from capillary vessels with diameter between 3 and 7 μm.

μm (Figure 1b). Based on our previously proposed approach (Bernabeu et al., 2018), we construct 3D flow models from the Col.IV binary image and run a whole-plexus blood flow simulation under the assumption of generalised non-Newtonian blood rheology (see the methods in Sec. 5.2.1). This is followed by simulations of RBC flow in designated regions of interest (ROIs) from the capillary bed (*e.g.* ROI-1, ROI-2 and ROI-3 in insets of Figure 1a) with inflow/outflow boundary conditions obtained from the whole plexus model (see the methods in Sec. 5.2.2). For full details of the computational framework modelling cellular blood flow, refer to Sec. S1 of the Supplementary Materials.

Our simulation recapitulates volume flow rates in the main artery and veins (running in the axial direction of the retina) of 0.36 μl/min and 0.17–0.19 μl/min, respectively. These flow rates are in good agreement with *in vivo* measurements recently performed in adult mouse retina of 0.39–0.59 μl/min and 0.24 μL/min, respectively (Joseph et al., 2019). The RBC velocities and fluxes calculated in the simulated ROIs are in the range 0–12.5 mm/s (Figure 1c) and 0–1400 RBC/s (Figure 1e), respectively. These results are validated against *in vivo* single-cell velocimetry data obtained in capillary vessels of diameter 3–7 μm (Joseph et al., 2019; Guevara-Torres et al., 2016). Both the simulation and experimental RBC velocities follow a skewed distribution and show good agreement with median values of 2.14 mm/s and 1.57 mm/s, respectively (p = 0.64, Figure 1d). The RBC fluxes are significantly higher in experiments than in simulations with median values of 120 RBC/s and 21 RBC/s, respectively (p = 0.046, Figure 1f). The main reason for the lower median observed in simulations is the presence of a number of vessel segments with zero or negligible RBC fluxes (Figure 1f), which will become the focus of study in the following section Sec. 2.2.

2.2 Strong association exists between RBC depletion and vessel regression in developing retinal vasculature

Having provided evidence of the broad range of RBC fluxes encountered in our ROIs, we now investigate a potential association between RBC dynamics and vessel regression. We classify ROI vessel segments into three groups (Figure 2a): the "lumenised" group shows positive signals in both Col.IV and ICAM2, featuring open lumina; the "stenosis" group shows positive signal in Col.IV and partial-positive/partial-negative signal in ICAM2, featuring vessel stenosis (an early stage in vessel regression as reported in (Franco et al., 2015); the "regression" group shows positive signal in Col.IV and negative signal in ICAM2, featuring vessel regression.

Further examination of our cellular flow simulations reveals that most RBC-depleted vessels in the simulation coincide with vessels in the regressed group (Figure 2a-b). To quantify this, we record the trajectories of all RBCs within each ROI throughout the simulation and study their density across the ROIs (Figure 2c). In general, a vessel segment with higher density represents good RBC perfusion, whereas those with low density indicate poor RBC perfusion, or RBC depletion. Subsequently, the time-averaged RBC flux within each vessel segment is calculated and assigned to the three groups under study (Figure 2d–f). Our analysis demonstrates that vessel segments in the lumenised group have significantly higher RBC fluxes than those in the stenosis group and the regression group ($p < 0.05$ for ROI-1 and $p < 0.01$ for ROI-2 and ROI-3, Figure 2d–f). Meanwhile, the difference in RBC flux between the stenosis group and the regression

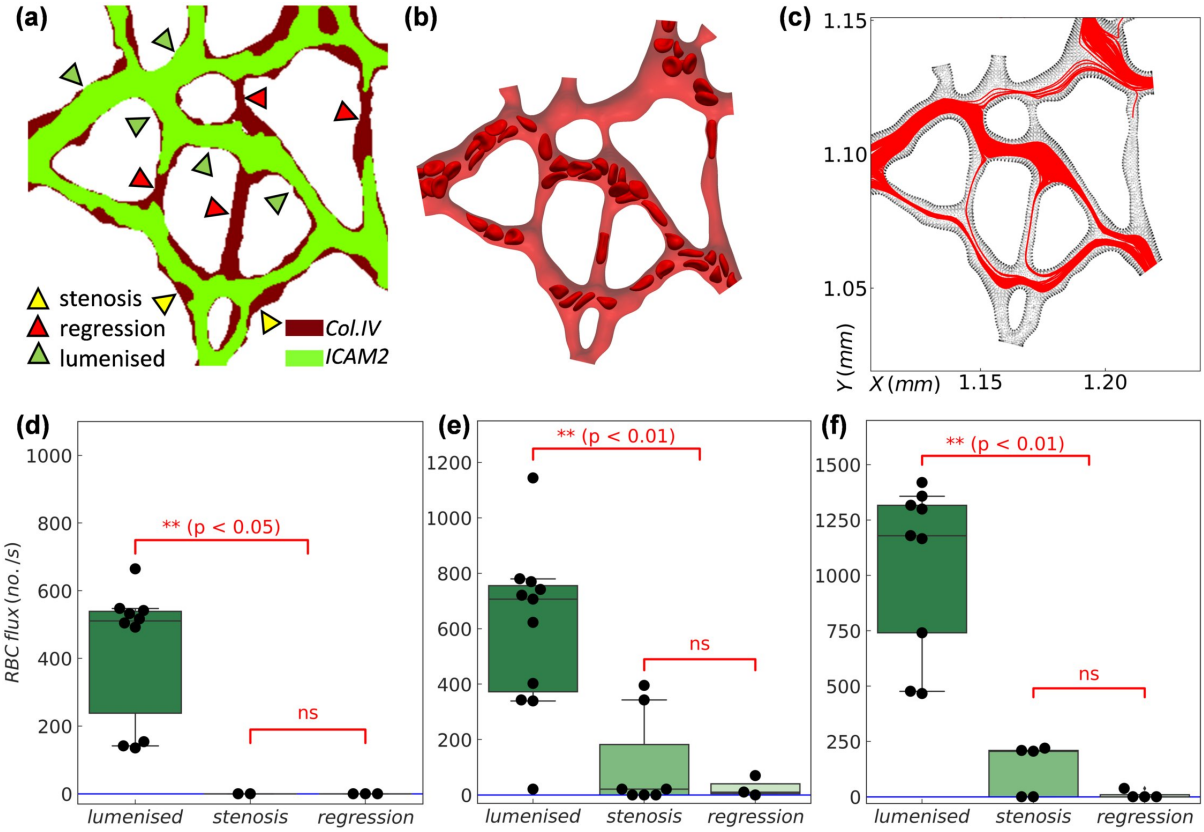

Figure 2: Association between RBC depletion and vessel regression in developmental mouse retina. (a) Characterisation of vessel segments in ROI-2 based on ICAM2 and Col.IV signals. The investigated vessels are divided into three groups, namely lumenised, regression and stenosis. (b) An exemplar simulation of the cellular blood flow in ROI-2. (c) Combined cell trajectories over time in ROI-2 throughout the simulation. (d–f) Quantification (Mann–Whitney U test) of time-average RBC fluxes in ROI-1, ROI-2 and ROI-3, respectively.

group is not significant ($p \gg 0.05$ for all ROIs, Figure 2d–f). These results support a strong association between RBC depletion and vessel regression.

2.3 *In vivo* validation of the effect of RBC perfusion on vascular remodelling in zebrafish caudal vein plexus

To provide experimental confirmation of the association between RBC depletion and vessel regression predicted by our computational model, we turned to the zebrafish model of vascular development, where simultaneous live imaging of vessel remodelling and RBC dynamics is possible. We chose the caudal vein plexus (CVP) for observation 48–72 hours post fertilisation (hpf), a period during which gradual remodelling of the plexus down to a single, well-defined vascular tube begins (Isogai et al., 2001). Comparison was made between control (ctl) morpholino oligomer (MO) fish with normal RBC perfusion (Figure 3a) and gata1 MO fish not carrying RBCs in their bloodstream (Figure 3b, see Sec. 5.1.2 for experimental details). Our time-lapse imaging of the CVP in ctl MO fish captures

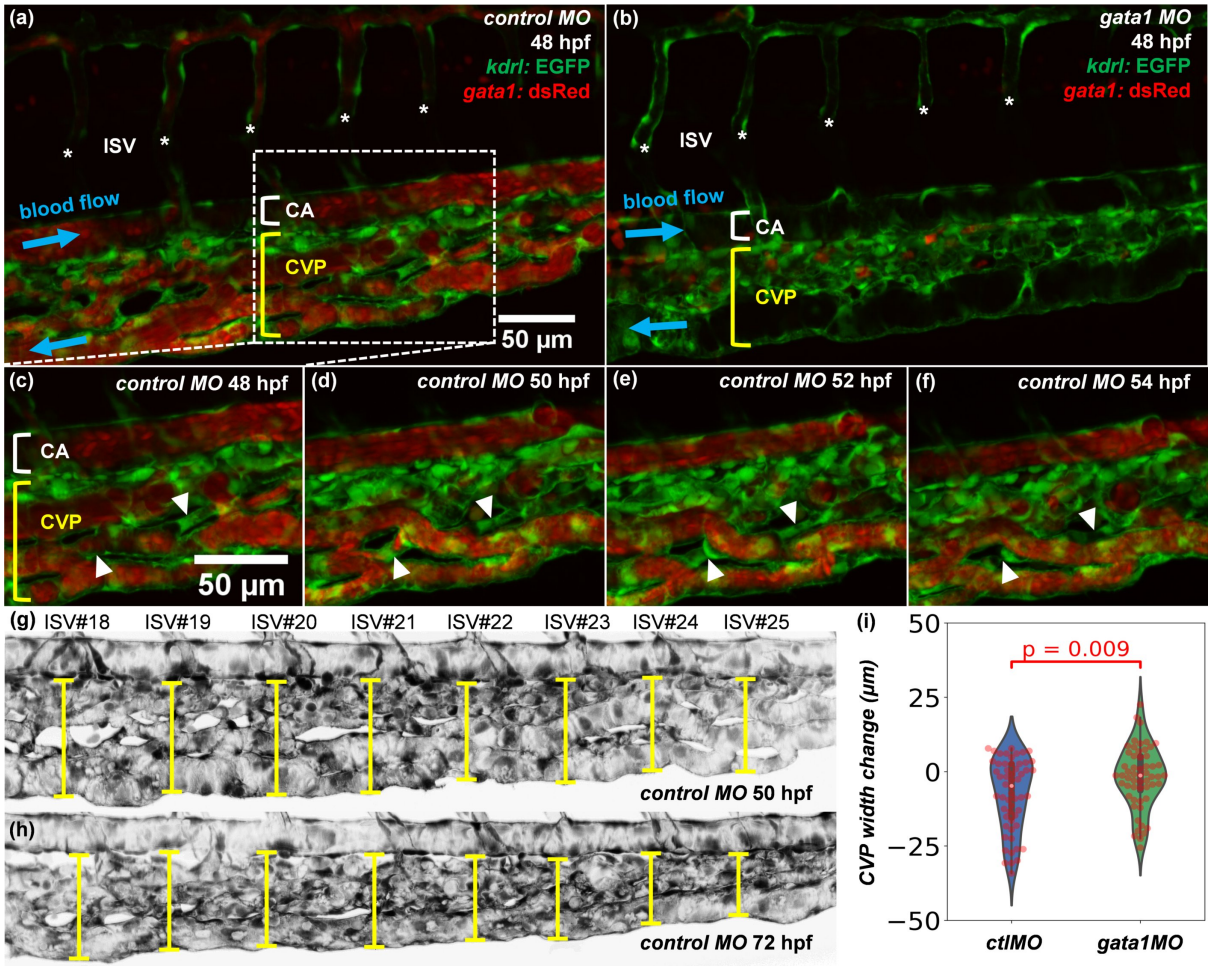

Figure 3: (a,b) Two exemplar caudal vein plexus (CVPs) from a 48 hpf ctl MO embryo (with RBC perfusion) and a 48 hpf gata1 MO embryo (*Tg(GATA-1:eGFP)*, without RBC perfusion). The intersegmental vessels (ISVs) are marked with asterisks, and the caudal artery (CA) is indicated by a square bracket. Note that the RBC precursors in (b) are located outside the vasculature and not circulating within the blood stream. (c–f) Time sequence showing vessel regression events observed in a region of interest extracted from the CVP of the zebrafish embryo in panel (a), where two vessel segments marked by white triangles are pruned over time (t = 48 hpf, 50 hpf, 52 hpf, 54 hpf). (g,h) Measurement of CVP widths at t = 50 hpf and t = 72 hpf along the anterior-posterior axis of a ctl MO embryo (Z-projection images) at positions given by eight consecutive ISVs (ISV 18–ISV 25). (i) Variation of the CVP widths between t = 50 hpf and t = 72 hpf calculated from measurements of the ctl MO group and the gata1 MO group (each containing 7 embryos). The statistical analysis is performed using Welch's T test.

heterogeneous RBC perfusion (Figure 3c) leading to multiple findings of intermittent and complete RBC depletion in vessel segments (Figure 3d) followed by vessel stenosis (Figure 3e) and eventual regression (Figure 3f). These *in vivo* findings therefore confirm our computational predictions in Sec. 2.2.

Next, we investigated how RBC deletion in gata1 MO fish impacts CVP remodelling at a network level. We measured CVP widths at standardised locations along the anterior-

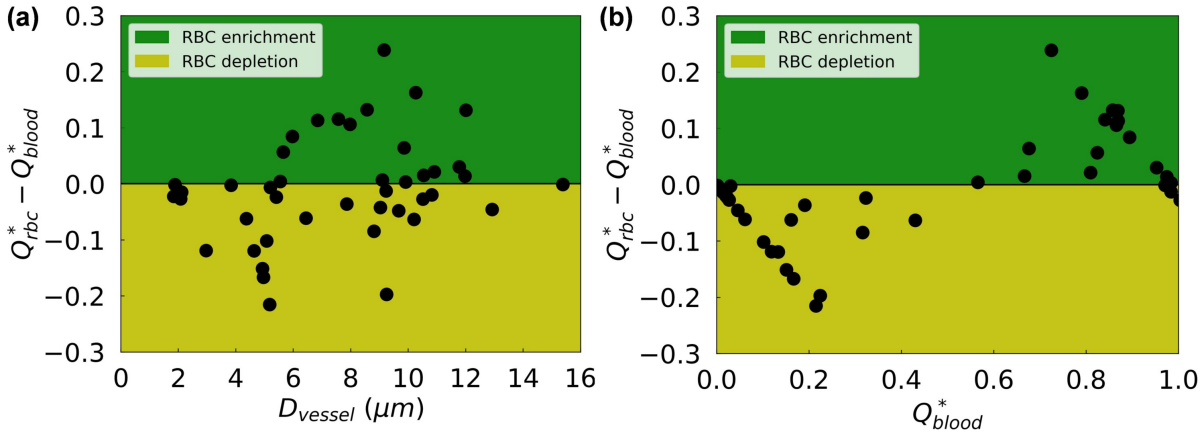

Figure 4: Quantification of RBC depletion in the developing retinal network. Q^*_{rbc} and Q^*_{blood} represent the normalised RBC flux and normalised blood flow in a given child vessel (with diameter D_{vessel}) relative to those in its parent vessel, respectively. The variable $\Delta Q^* = Q^*_{rbc} - Q^*_{blood}$ serves as a disproportionality index of flow-mediated RBC partitioning, based on the sign of which the vessels are classified as "RBC-depletion" (negative ΔQ^*, yellow patch) and "RBC-enrichment" (positive ΔQ^*, green patch). The disproportionality indices for all investigated vessel segments are sorted against (a) vessel diameter D_{vessel} and (b) normalised blood flow Q^*_{blood}, respectively. The analysed vessel segments in this plot are extracted from the three ROIs in Figure 1.

posterior fish axis given by the position of eight consecutive intersegmental vessels (ISV) beginning at ISV 18, for both the ctl MO and gata1 MO groups ($n = 7$ each group) at 50 hpf and 72 hpf (see Figure 3g–h for an example fish from the ctl MO group). During this period of time, substantial remodelling leading to narrowing of the plexus is observed in the wild type (agreeing with Isogai et al., 2001). Furthermore, significantly larger reduction of CVP width in the ctl MO group is found in comparison to the gata1 MO group, with mean reductions 7.64 μm and 2.01 μm, respectively ($p < 0.01$, Figure 3i). This several-fold difference implies that the presence of RBCs is necessary for normal CVP remodelling 50–72 hpf, and therefore the heterogeneity in RBC perfusion described in Figure 3c–f does play a role in orchestrating network-level remodelling.

2.4 Network RBC depletion not predictable by vessel diameter

The absence of RBCs in some vessel segments in both our simulations and experiments poses a crucial question about cellular flow in developmental vascular network: what is the governing mechanism that determines which vessels to be perfused with cells and which to be devoid of? It is tempting to speculate that the pattern of vessel RBC depletion is merely a size-exclusion effect; namely, certain vessel segments are simply too narrow to allow cells to pass through. However, the vessel diameters encountered in the present simulations (about 2–16 μm) are unlikely to be the dominant factor affecting RBC transit, since the high deformability of RBCs under physiological conditions enables them to pass through exceedingly small passages as narrow as 1–2 μm (Freund, 2013; Salehyar and Zhu, 2016, 2017; Lu and Peng, 2019). Indeed, the material model adopted for the RBC membrane allows the cells to deform and adopt highly elongated shapes to flow through all

narrow capillaries that they enter in our simulations (with one exception only), whereas some larger vessels are devoid of RBCs (see Movies 1-3 of the Supplementary Materials).

Furthermore, we evaluate the degree of RBC enrichment/depletion by examining the sign and magnitude of $\Delta Q^* = Q^*_{rbc} - Q^*_{blood}$ (positive for enrichment and negative for depletion, see definitions in Sec. 5.3.1) against vessel diameter D_{vessel} for all child branches studied here (44 in total, Figure 4a). RBC depletion occurs throughout the whole range of vessel sizes investigated ($D_{vessel} \in [2, 16]\,\mu$m). Notably, for one child branch with $D_{vessel} \approx 9\,\mu$m (larger than the physiological RBC diameter), ΔQ^* is -0.2, indicating a 20% reduction in RBC transit. Based on these findings, we conclude that RBC depletion is not a size-exclusion effect. Meanwhile, it is found that RBC enrichment happens only in medium/large vessels ($D_{vessel} > 5\,\mu$m). Within the intermediate diameter range $D_{vessel} \in [5, 12]\,\mu$m, the vessels have nearly equal chances of being enriched or depleted.

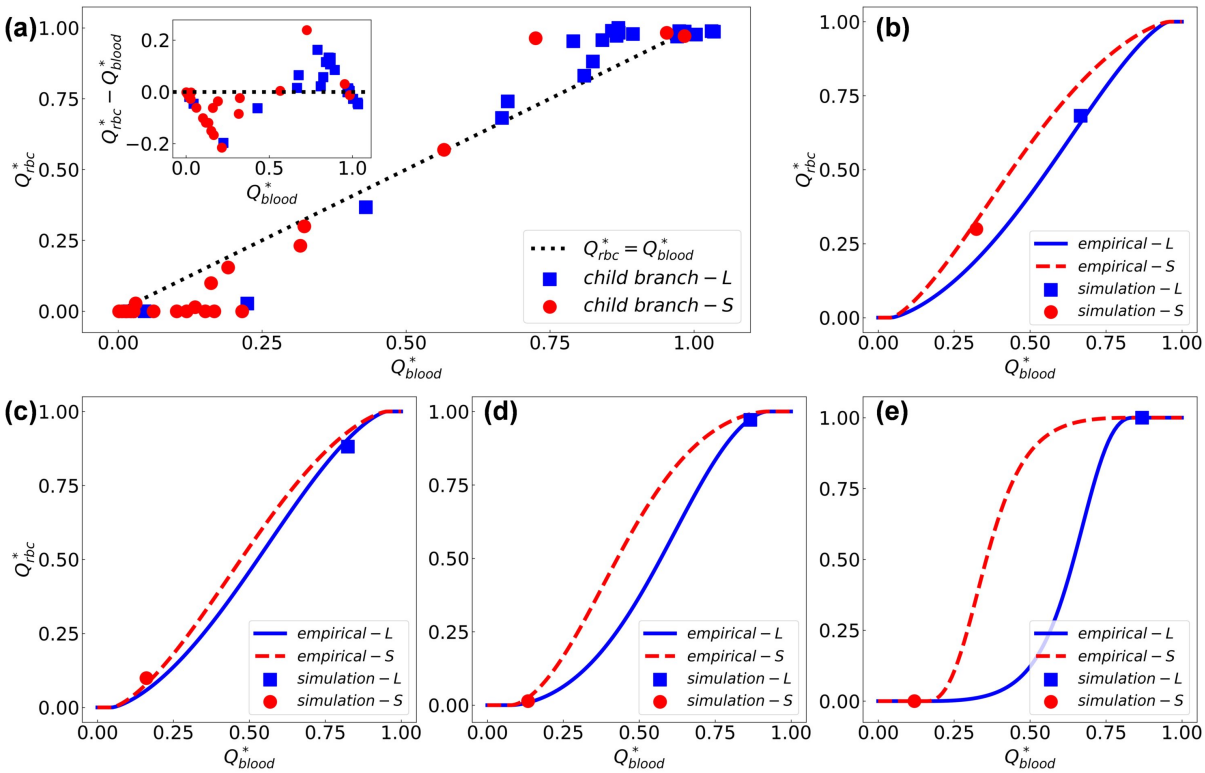

Figure 5: Comparison of simulation data with empirical predictions by the phase separation model (PSM, (Pries et al., 1989, 2003)). (a) Simulation data of fractional RBC flux Q^*_{rbc} against fractional blood flow Q^*_{blood} in the relatively larger child branch "L" (blue squares) and smaller child branch "S" (red circles) from all investigated bifurcations. The inset shows similar results as in Figure 4b (characterising the disproportionality index $\Delta Q^* = Q^*_{rbc} - Q^*_{blood}$ against Q^*_{blood}), but with additional information of relative vessel size for child branches in each bifurcation. The black dotted line represents a linear hypothesis for Q^*_{rbc} and Q^*_{blood} in the absence of plasma skimming. (b–e) Four exemplar bifurcations in which the simulation data (squares and circles) agree well with empirical predictions (solid lines) for both the "L" and "S" child branches.

Table 1: Errors of empirical prediction by the phase separation model (Pries et al., 1989, 2003) in comparison to our simulation data. "ROI" represents region of interest; "BOI" represents bifurcation of interest; "CB" represents child branch. "L" and "S" refer to the relatively larger and smaller child branch within each bifurcation, respectively.

ROI	CB	BOI-1	BOI-2	BOI-3	BOI-4	BOI-5	BOI-6	–	–
1	L	0.44%	0.22%	2.38%	0.0%	0.0%	1.12%	–	–
1	S	2.26%	3.47%	0.0%	2.89%	1.7%	0.0%	–	–
ROI	CB	BOI-7	BOI-8	BOI-9	BOI-10	BOI-11	BOI-12	BOI-13	BOI-14
2	L	2.32%	1.35%	4.74%	0.28%	0.0%	2.5%	1.21%	0.72%
2	S	2.68%	0.0%	9.19%	1.08%	0.0%	1.97%	4.29%	0.0%
ROI	CB	BOI-15	BOI-16	BOI-17	BOI-18	BOI-19	BOI-20	BOI-21	BOI-22
3	L	6.78%	1.16%	3.49%	1.64%	3.03%	1.3%	11.86%	1.58%
3	S	5.28%	0.0%	9.02%	0.0%	2.78%	0.0%	17.62%	0.44%

2.5 Plasma skimming as a mechanism for RBC depletion in developing vascular network

Having demonstrated that size-exclusion effect alone is not sufficient to explain the RBC depletion observed in Sec. 2.2, we now turn our attention to potential haemodynamic mechanisms. First, we observe that characterising $\Delta Q^* = Q^*_{rbc} - Q^*_{blood}$ against the haemodynamic indicator Q^*_{blood} does satisfactorily separate the RBC-depletion zone from the RBC-enrichment zone (Figure 4b). This finding is in line with the plasma skimming effect described by empirical models such as the widely-employed Phase-Separation Model (PSM, see a detailed introduction in Sec. 5.3.2), first proposed by Pries and co-workers (Pries et al., 1989, 1990).

To qualitatively assess the agreement between our data and the PSM, we plot the fractional RBC fluxes Q^*_{rbc} in individual child branches (44 studied here) of any divergent bifurcation against their fractional blood flow Q^*_{blood} (Figure 5a). The distribution is indeed reminiscent of the sigmoidal relationship predicted by the PSM, where $Q^*_{rbc} > Q^*_{blood}$ for $Q^*_{blood} > 0.5$ up to a threshold where $Q^*_{rbc} = 1$ (and the opposite effect for $Q^*_{blood} < 0.5$ down to $Q^*_{rbc} = 0$). Furthermore, albeit with occasional exceptions, the child branch relatively smaller in size (red circles) within a bifurcation tends to receive lower blood flow and consequently fewer RBCs, whereas the larger child branch (blue squares) is more likely to have higher blood flow and attract more RBCs (inset of Figure 5a). Note that "smaller" or "larger" here is a relative notation between the two child branches within a bifurcation, instead of a measure of the absolute vessel size.

Furthermore, we compare our simulation data at each bifurcation with the prediction given by the PSM model (Equations (1)–(6)). We observe errors of less than 5% for 18 out of 22 bifurcations (see Table 1 for complete error evaluation). Figure 5b–e demonstrate four cases of good agreement. In the first bifurcation, both child branches have considerable proportions of blood flow (roughly 30% and 70%, respectively) and are well-perfused by RBCs, with the fractional RBC fluxes matching the PSM predictions (Figure 5b). In the second bifurcation, most RBCs ($Q^*_{rbc} \approx 90\%$) enter the relatively larger child branch as it receives more than 80% of the blood flow from the parent branch (Figure

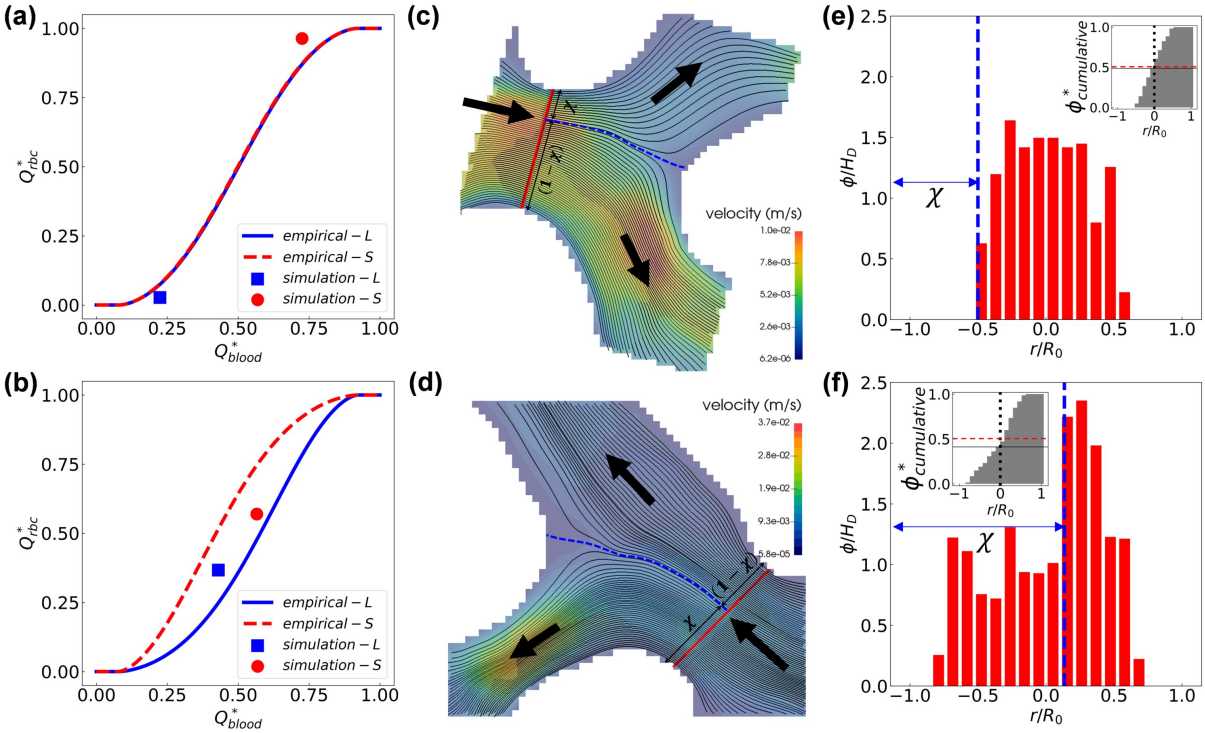

Figure 6: Deviation of simulation data from the empirical model due to the asymmetry of haematocrit profile in the parent branch. (a–b) Two exemplar divergent bifurcations for which the simulation data (circle dots) deviate from PSM predictions (solid lines). (c–d) Visualisation of the flow streamlines separated into the child branches on the mid-plane of the bifurcation (extracted from the 3D simulation). The blue dashed line indicates the location of the separation surface. (e–f) Cross-sectional haematocrit profile in the parent branch, at a position marked by the red solid line in (c–d). The blue dashed line corresponds to the separation surface of flow streamlines as in (c–d). The insets of (e–f) show the cumulative haematocrit distribution corresponding to the haematocrit profile.

5c). In the third and fourth bifurcations (Figure 5d–e), the smaller child branch is nearly devoid of cells as the relatively larger branch attracts almost all RBCs from the feeding vessel owing to its predominantly higher proportion of blood flow ($Q^*_{blood} > 85\%$). Larger than 5% deviations from the PSM are observed in the remaining 4 of the 22 bifurcations studied (see Figures S1–S3 in Sec. S2 of the Supplementary Materials).

Shown in Figure 6a–b are two cases where the simulated RBC fluxes in the bifurcation deviate from the empirically predicted values. Interestingly, the RBC flux contrast between the two child branches is slightly underestimated by the PSM model in the first case (Figure 6a) whereas it is substantially overestimated in the second case (Figure 6b). To investigate these disagreements, we examine the flow streamlines in the mid-plane of the bifurcation and calculate the relative distance χ of the stagnation streamline separating the flow entering the left branch from that entering the right branch (Figure 6c–d). Clearly, the higher-flow branch (child branch with larger Q^*_{blood}) receives proportionally more streamlines from the parent vessel and should therefore receive more RBCs accordingly provided that the cells are axisymmetrically distributed in the parent branch (as assumed by the empirical model of PSM).

Next, we investigate whether the assumption of haematocrit axisymmetry by the PSM holds in our simulations. To this end, we calculate the cross-sectional distribution of RBCs in the parent branch. We find clearly asymmetric distributions, especially for case two (Figure 6e–f). In both cases, the haematocrit profile is skewed towards the right-hand side of the bifurcation, with a cumulative haematocrit to the left-hand side of the vessel centreline either slightly or substantially smaller than 0.5 (see insets of Figure 6e–f). Such haematocrit asymmetry makes the downstream child branch on the right-hand side inherently advantageous for RBC intake (hereafter referred to as haematocrit-favoured branch). In case one, the higher-flow branch coincides with the haematocrit-favoured branch, resulting in enhanced RBC flux difference between the two child branches; whereas in case two, the higher-flow branch differs from the haematocrit-favoured branch, thus attenuating the RBC flux difference. A full description of the mechanism leading to this skewness, which originates from the interplay between the complex geometry and the emerging RBC behaviour in the microvasculature, is out of the scope of the present study and will be explored in future work.

3 Discussion

Earlier studies have extensively explored the effect of blood flow on cardiovascular development and it is well accepted that haemodynamic cues are essential for vascular patterning (Lucitti et al., 2007, Chen et al., 2012, Kochhan et al., 2013). Previous work by our groups further established the pivotal role of regional WSS differences, which were found to locally modulate the polarised migration of ECs into high-shear vessel segments and cause the regression of adjacent segments experiencing low shear (Franco et al., 2015, 2016; Vion et al., 2018). However, because the quantification of WSS in these studies relied on mathematical flow models assuming simplified blood rheology, the question of how the presence of RBCs and their profound impact on microvascular haemodynamics affect vascular remodelling has not been addressed. Recent simulations of cellular blood flow in single microvessels have shown that RBCs can non-trivially modify both the mean and oscillatory components of local WSS (Freund and Vermot, 2014; Hogan et al., 2019), thereby suggesting a salient impact of RBCs on the mechanotransduction of fluid forces during angiogenesis. Based on these findings, we hypothesise that RBCs in the developing mouse retina play an active role in the course of vascular patterning towards a functional network *via* altering WSS spatially and temporally.

In the current study, we simulated RBC dynamics in the vascular plexus of a wild-type mouse retina at P5. The computed RBC velocities are in good agreement with *in vivo* measurements made in adult mouse retinas (Joseph et al., 2019; Guevara-Torres et al., 2016). However, differences arise in terms of RBC fluxes (more heterogeneous distribution with lower median value, Figure 1f). We attribute this discrepancy to structural differences between the developmental stage simulated and the adult stage considered for validation. We hypothesise that as the primitive network remodels, the simulated RBC fluxes will become closer to the *in vivo* measurements in adult mice. Future advances in live imaging of the mouse retina model will contribute to elucidate this process.

Other sources of uncertainty in the current simulations remain to be quantified. First, the discharge haematocrit at the inlets of all ROIs was fixed at 20% for consistency.

This value is in line with the average microvascular haematocrit level reported in the literature, *i.e.* $23\% \pm 14\%$ by (Pries and Secomb, 2008), but may not necessarily reflect the haematocrit levels of individual mice studied in (Joseph et al., 2019; Guevara-Torres et al., 2016) and used for validation in our study. Second, the flow in realistic microvessels with smaller lumen size than the RBC diameter is typically impeded due to the close contact of RBCs with the endothelial surface layer (ESL, consisting of glycocalyx and/or cilia), whereas in our present *in silico* model such microscopic structures on the vessel wall are not considered. Prior studies in glass tubes where the ESL was absent demonstrated a two-fold decrease in flow resistance when compared to *in vivo* conditions (Pries et al., 1994, 1997).

Our simulations of cellular blood flow reveal a previously unreported heterogeneity in RBC perfusion throughout the developing vascular network, where a number of plasma vessels exist with rare RBC transit over time, and a strong association between RBC depletion and vessel regression. From a mechanistic point of view, the effective viscosity in neighbouring RBC-depleted and RBC-enriched branches can differ substantially. Such disparity in viscosity will enhance the regional WSS difference between neighbouring branches, which can in turn promote the pruning of the vessel segment depleted of RBCs according to previously reported mechanisms (Franco et al., 2015). We provide further experimental confirmation of these findings in the developmental zebrafish model, which is amenable to live imaging. In agreement with Lucitti *et al.* (Lucitti et al., 2007), we show that the presence of RBCs is necessary for effective remodelling at a whole plexus level. Furthermore, we extend the conceptual model by demonstrating that intermittent and complete RBC depletion selects vessels for regression.

To fully understand the RBC perfusion within the developing mouse retina, we asked the question: what is the mechanism behind RBC depletion/enrichment in the primitive network? Quantification of RBC fluxes against vessel diameter and blood flow in individual bifurcations rules out vessel-size exclusion as the primary factor. Instead, the empirical model by Pries *et al.* (Pries et al., 1989, 2003) based on the plasma skimming effect explains the uneven partitioning of RBC fluxes satisfactorily in 18 out of 22 cases, therefore implying that the distribution of RBCs within the developing network is flow-mediated rather than geometry-dominant.

For the 4 cases where predictions of the empirical model do not satisfactorily match the simulation data, we find considerable haematocrit asymmetry in the cross-sections of the feeding branches, which is against the central assumption of axisymmetric haematocrit profile by the model. This makes accurate prediction of the RBC perfusion in a given vascular network challenging without certain knowledge of cross-sectional cell distributions. Our observation of haematocrit-favoured and haematocrit-unfavoured vessel branches at microvascular bifurcations is in line with recent *in vitro* findings of reversion of the classic haematocrit partitioning which otherwise always favours the higher-flow branch (Sherwood et al., 2014; Clavica et al., 2016; Shen et al., 2016). Similar reverse partitioning was reported by simulations of cellular blood flow in microvascular networks with vessel diameters designed following Horton's law (Balogh and Bagchi, 2018). Our group has recently identified reduced interbifurcation distance and complex branching topology as sources of haematocrit asymmetry in the context of tumour blood flow. Furthermore, we propose a role for the resulting abnormal partitioning in establishing tumour tissue hypoxia (Bernabeu et al., 2019).

The asymmetry not only applies to the haematocrit profile, but also the velocity profile. For a majority of microcirculatory models, the Poiseuille law has been employed to simplify the haemodynamics and reduce computational cost, manifested by parabolic velocity profiles featuring a peak velocity at the centreline of microvessels. Our results counter such a simplification, as the velocity profile in a capillary vessel can significantly deviate from a parabola and become skewed over time in the presence of travelling RBCs (Figure S4 in Sec. S3 of the Supplementary Materials). Similar deviation of velocity profiles has also been confirmed by imaging data from living mouse retina, where a 39% error in flow estimation was reported if assuming a parabolic profile (Joseph et al., 2019).

The co-existence of asymmetries in the velocity and the haematocrit profiles adds to the complexity of network analysis in the context of RBC perfusion, as it turns out unclear whether a general rule holds to determine the preferred child branch when the flow split and haematocrit distribution contradict each other regarding path preference. This may introduce extra stochastic effects in the remodelling of primitive vasculature, which remains to be explored. In addition, one should bear in mind the prominence of network effect for a microcirculatory system, which non-trivially modulates the haemodynamics within individual microvessels.

4 Concluding remarks

In summary, our study reports a new mechanism for enhancement of the WSS differences driving vascular remodelling during development. These enhanced differences arise due to the highly heterogeneous distribution of RBCs within the primitive plexus, which is primarily governed by the plasma skimming effect. Additionally, we speculate that vascular remodelling driven by the principle of removing RBC-poor vessels from the primitive vasculature will lead to a network layout that avoids portions of the tissue being vascularised but poorly oxygenated. This RBC-driven process, which is highly dynamical and emerging in nature, can importantly contribute to the optimal patterning of vascular networks during development. Beyond these findings, our study also has important implications for the mathematical modelling of microvascular haemodynamics in general. In a network of microvessels, multiple effects inexplicable by continuum flow models (albeit widely employed for modelling blood flow in complex vascular networks by existing studies) occur owing to the particulate nature of blood, *i.e.* essentially a suspension of RBCs. Conventional assumptions such as Poiseuille law, velocity-/haematocrit-profile symmetry, spatial-/time-average accuracy are all subject to scrutiny when quantifying flow variables such as effective viscosity and WSS in the microcirculation, especially for vessels with a lumen smaller than the undeformed size of an RBC (*i.e.* 6.2–8.2 μm).

5 Materials and methods

5.1 Mouse and zebrafish experiments

5.1.1 Preparation of mouse retina for binary mask acquisition

The mouse strain used in the present study was C57/BL6J. Mice were maintained at the Max Delbrück Center for Molecular Medicine under standard husbandry conditions. An-

imal procedures were performed in accordance with the animal license X9005/15. Mouse eyes were collected at P5 and fixed with 4% PFA in PBS for 1 h at 4°C, and retinas were then dissected in PBS. Blocking/permeabilisation was performed using Claudio's Blocking Buffer (CBB; Franco et al., 2013), consisting of 1% FBS (Gibco), 3% BSA (Sigma-Aldrich), 0.5% Triton X-100 (Sigma-Aldrich), 0.01% sodium deoxycholate (Sigma-Aldrich), and 0.02% sodium azide (Sigma-Aldrich) in PBS at pH 7.4 for 2 h with rocking at 4°C. Primary antibodies were incubated at the desired concentration in 1:1 CBB/PBS with rocking at 4°C overnight and secondary antibodies were incubated at the desired concentration in 1:1 CBB/PBS for 2 h at room temperature. Retinas were mounted on slides using Vectashield mounting medium (H-1000; Vector Labs).

The following primary and secondary antibodies were used *in vivo*: collagen IV (ref 2150-1470, rabbit; 1:400; AbD Serotec) and ICAM2 (ref 553326, rat; 1:200; BD Biosciences), anti-Rat Alexa 488 (ref A21208, donkey 1:400, Invitrogen), anti-Rabbit Alexa 568 (ref A10042, donkey 1:400, Invitrogen). Complete high-resolution three-dimensional rendering of whole mount retinas were taken using a LSM 780 inverted microscope (Zeiss) equipped with a Plan-Apochromat 63×/1.4 NA DIC objective. Images were taken at room temperature using Zen 2.3 software (Zeiss). Tiled scans of whole retinas were analysed with ImageJ to generate binary masks of ICAM2 and Collagen IV.

5.1.2 Morpholino oligomers, zebrafish husbandry and imaging

Morpholino oligomer (MO) against *gata1* Morpholino (gata1 MO) as described in (Amigo et al., 2009) (sequence 5'-CTGCAAGTGTAGTATTGAAGATGTC-3') was injected at 8 ng/embryo following (Hogan et al., 2009). A control MO (ctl MO) served the standard control Morpholino with the sequence 5'- CCTCTTACCTCAGTTACAATTTATA-3' targeting a human beta-globin intron mutation. The control was injected at similar amount of 8 ng/embryo. Zebrafish (*Danio rerio*) were raised and staged as previously described in (Kimmel et al., 1995). For growing and breeding of transgenic lines, we complied with regulations of the animal ethics committee at the MDC Berlin (Aleström et al., 2019).

Embryos were anaesthetised in 0.014% tricaine (Tricaine Pharmaq 1000mg/g, PHARMAQ Limited), mounted in plastic petri dishes (94x16 mm - Sarstedt Ref#82.1473) containing 0.014% tricaine, and bathed in E3 media containing 0.007 (0.5x) tricaine and 0.003% PTU. Imaging was performed on an upright 3i spinning-disc confocal microscope using Zeiss Plan-Apochromat 20x/1.0 NA water-dipping objectives. Screening of embryos was performed using a Leica M205 FA stereomicroscope with filter set ET GFP M205FA/M165FC.

5.2 Numerical simulation

5.2.1 Whole-plexus simulation

A three-dimensional (3D) flow model of the luminal surface (Figure 7b) is reconstructed from the Col.IV binary mask (Figure 7a) using the open-source software *PolNet* (Bernabeu et al., 2018), under the assumption of circular vessel cross-sections. The flow domain is then discretised into uniform cubic lattice grids with a size of Δx, whose value is chosen to be $\Delta x = 0.5\,\mu$m for the mouse retina used here such that the flow can be accurately

Table 2: Key parameters of the whole-plexus simulation using the non-Newtonian Carreau-Yasuda (NNCY) rheology model (Boyd et al., 2007; Bernabeu et al., 2014).

Parameter	Description	Value	Unit	Comment or reference
D_{vessel}	vessel diameter	variable	μm	locally mapped by *PolNet*
Δx	lattice size	0.5	μm	calculated by *PolNet*
Δp	ocular perfusion pressure	55	mmHg	(Bernabeu et al., 2014)
$\bar{u}$	flow mean velocity	variable	m/s	averaged over cross-section
Q	volume flow rate	variable	m^3/s	$Q = \bar{u}\pi D_{vessel}^2/4$
$\dot{\gamma}$	shear rate	variable	1/s	solved by *HemeLB*
$\eta(\dot{\gamma})$	shear-thinning viscosity	variable	mPa s	$\eta(\dot{\gamma}) = \eta_\infty + \frac{(\eta_0-\eta_\infty)}{[1+(\lambda\dot{\gamma})^a]^{(1-n)a}}$
η_0	constant	14.49	mPa s	viscosity under low-shear
η_∞	constant	3.265	mPa s	viscosity under high-shear
λ	constant	0.1839	s	fitting parameter
n	constant	0.4136	-	fitting parameter
a	constant	2.707	-	fitting parameter

solved throughout the reconstructed network for reliable results of flow rates and wall shear stresses even in the smallest lumenised vessels.

The whole-plexus simulation in the reconstructed network adopts the non-Newtonian Carreau-Yasuda rheology model (NNCY; Boyd et al., 2007) following our previous approach (Bernabeu et al., 2014), where blood is modelled as a generalised Newtonian fluid (homogeneous shear-thinning liquid). By imposing a physiological ocular perfusion pressure (OPP) between the arteriole and venules, a steady flow within the vascular plexus is solved (Figure 7c) to provide boundary conditions for subsequent RBC simulations in designated regions of interest (ROIs) of the plexus. OPP = 55 mmHg is chosen for the present simulation based on a literature survey and sensitivity analysis conducted in (Bernabeu et al., 2014). Table 2 provides key parameters of the whole-plexus simulation.

5.2.2 RBC simulation in network subsets

To create RBC simulations in ROIs of the retinal network where evident vessel regression events are observed (*e.g.* Figure 7d), we first clip the designated ROI from the whole-plexus as a geometric subset (Figure 7e). For a ROI subset with N open boundaries, we set up $(N-1)$ Poiseuille velocity inlets/outlets (where parabolic velocity profiles are imposed with a centreline velocity of $\hat{u}$) and one pressure outlet (where a reference pressure $p_{out} = 0$ is set). The velocity boundary conditions are obtained from the NNCY simulation through measuring local flow rates Q in vessels of interest and subsequently calculating $\hat{u}$ from Q under the assumption of Poiseuille flow, following $\hat{u} = 2\bar{u} = 2Q/\pi D_{vessel}^2$. With all the above boundary conditions set (see Table 3), a plasma flow simulation is initiated in the ROI with the fluid viscosity equal to that of plasma η_{plasma}. Once steady flow is achieved and the velocity field is verified against the NNCY simulation, we populate the ROI with RBCs which are continuously fed at a discharge haematocrit of 20 % from all inlets of the subset network (Figure 7f).

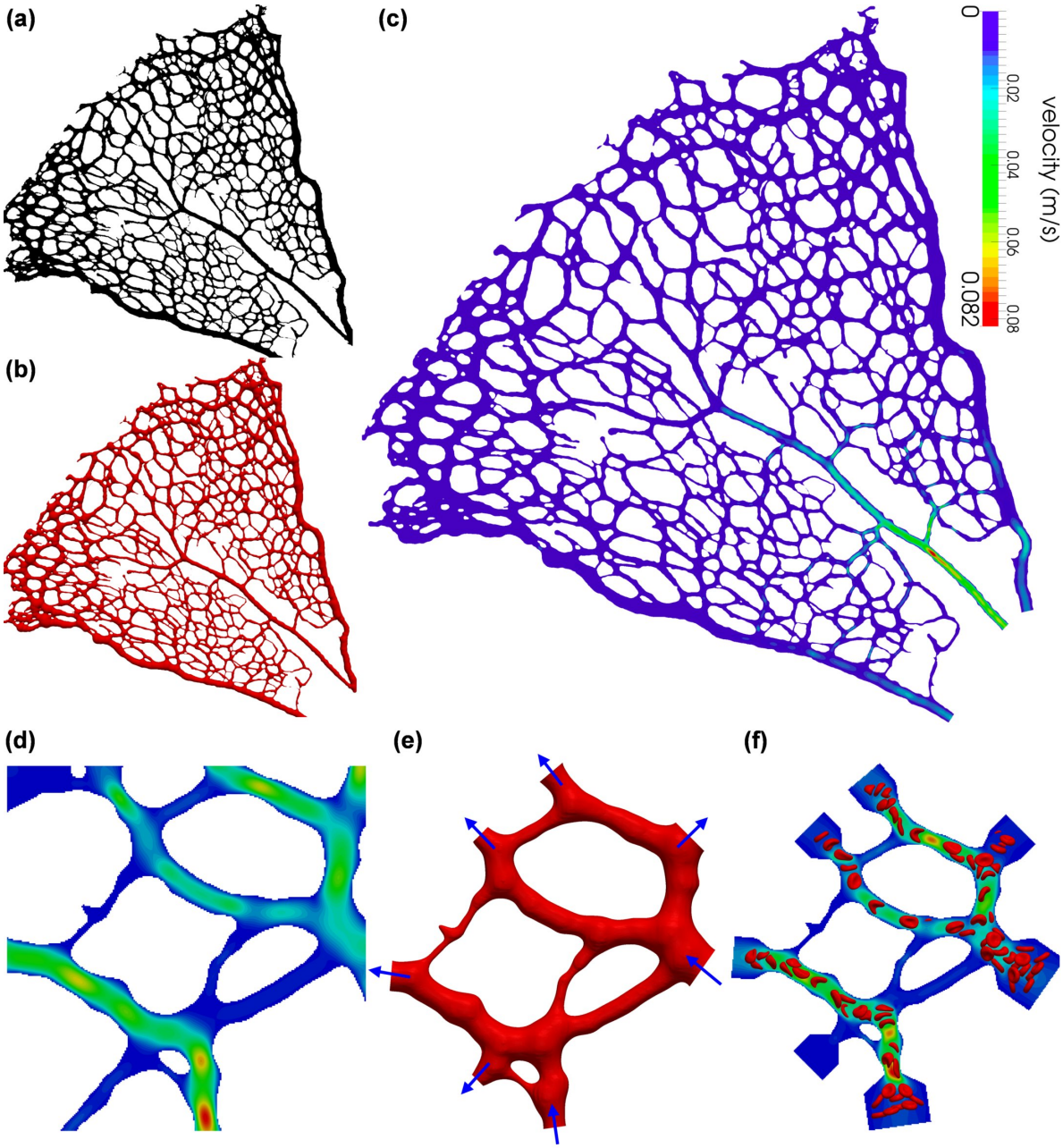

Figure 7: Procedure of model configuration and simulation setup for simulating cellular blood flow in designated regions of interest (ROIs) from the vascular plexus of mouse retina. (a) Binary image of the vascular plexus stained for Col.IV. (b) Reconstructed whole-network geometry of the vessel lumina surface from (a). (c) Velocity field within the retinal network resolved by a flow model applying the non-Newtonian Carreau-Yasuda (NNCY) blood rheology in (b). (d) Zoomed in velocity field for a designated ROI in (c). (e) Clipped ROI subset from the whole-network geometry with inlets/outlets indicated by the inward/outward arrows. (f) Cellular flow simulation in the designated ROI imposing inflow/outflow and pressure boundary conditions extracted from (d).

Table 3: Boundary conditions for RBC simulations in designated subsets of the retinal network, namely ROI-1, ROI-2 and ROI-3. $\hat{u}$ represents the centreline velocity at the selected cross-section (circular) of a given vessel that serves as the inlet/outlet of the ROI and p is a reference pressure. $\hat{u}$ is set as positive for inlets and negative for outlets.

ROI	Inlet/Outlet	Boundary type	Value	Unit	D_{vessel} (μm)
1	$\hat{u}_{in1}$	velocity	11.710	mm/s	8.0
	$\hat{u}_{in2}$	velocity	3.756	mm/s	15.7
	$\hat{u}_{out1}$	velocity	-0.774	mm/s	5.4
	$\hat{u}_{out2}$	velocity	-6.164	mm/s	10.6
	$\hat{u}_{out3}$	velocity	-5.209	mm/s	7.1
	$\hat{u}_{out4}$	velocity	-4.829	mm/s	10.4
	p_{out5}	pressure	0	mmHg	14.5
2	$\hat{u}_{in1}$	velocity	4.222	mm/s	19.0
	$\hat{u}_{in2}$	velocity	1.201	mm/s	5.5
	$\hat{u}_{in3}$	velocity	6.367	mm/s	7.8
	$\hat{u}_{out1}$	velocity	-11.658	mm/s	10.3
	$\hat{u}_{out2}$	velocity	-7.182	mm/s	8.6
	$\hat{u}_{out3}$	velocity	-0.514	mm/s	7.3
	$\hat{u}_{out4}$	velocity	-0.113	mm/s	6.8
	p_{out5}	pressure	0	mmHg	8.9
3	$\hat{u}_{in1}$	velocity	1.171	mm/s	7.1
	$\hat{u}_{in2}$	velocity	10.277	mm/s	13.5
	$\hat{u}_{in3}$	velocity	0.049	mm/s	6.9
	$\hat{u}_{in4}$	velocity	0.002	mm/s	2.4
	$\hat{u}_{out1}$	velocity	-14.913	mm/s	8.8
	$\hat{u}_{out2}$	velocity	-30.298	mm/s	4.7
	p_{out3}	pressure	0	mmHg	2.2

5.3 Data analysis

5.3.1 Vessel selection and quantification of RBC flow

For the study of RBC perfusion within the ROI subsets, we locate all divergent bifurcations (*i.e.* consisting of one parent branch and two downstream child branches) encountered by the cellular flow in each ROI *via* exhaustively examining the flow directions (identical between the whole-plexus simulation and the ROI plasma flow simulation) in every single vessels segment (Figure 8a–c). Only vessel branches from these divergent bifurcations are selected for statistical analysis to ensure independent representation of the systematic RBC partitioning occurring in the network. In total, 22 divergent bifurcations and 54 independent vessel segments (excluding 12 repetitive branches) are identified from the three ROIs.

To quantify the partitioning of RBCs at each divergent bifurcation (Figure 8d–f), we introduce two variables following the practice of (Pries et al., 1989; Balogh and Bagchi, 2018): the first one is Q^*_{blood}, denoting the proportion of blood flow that a given child branch receives from its parent branch ($0 \leq Q^*_{blood} \leq 1$); the other is Q^*_{rbc}, denoting the

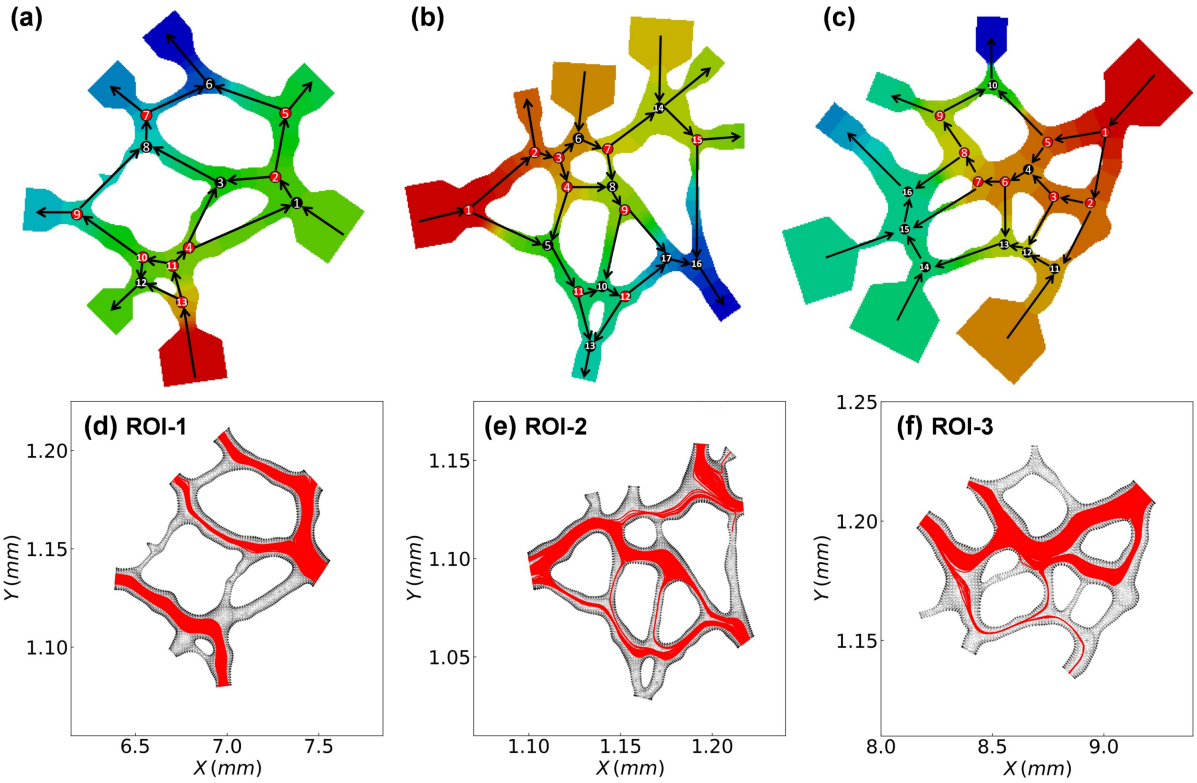

Figure 8: (a–c) Flow patterns detected within ROI-1, ROI-2 and ROI-3, respectively. The arrows within the ROIs indicate the flow directions in individual vessel segments, and the background contour indicates the pressure field, with a warmer colour (*e.g.* red) representing a higher pressure. The divergent bifurcations within each ROI are marked with red circles and the convergent ones with black. (d–f) Combined cell trajectories in the ROIs throughout RBC simulations lasting for 0.33 s each.

proportion of RBC flux likewise ($0 \leq Q^*_{rbc} \leq 1$). If $Q^*_{rbc} > Q^*_{blood}$, the child branch is receiving more RBCs than linear allocation and we define it as an "RBC-enriched" vessel; if $Q^*_{rbc} < Q^*_{blood}$, the child branch is receiving fewer RBCs than the linear hypothesis and we define it as an "RBC-depleted" vessel.

5.3.2 Evaluation of simulation data against the phase separation model

Several models have been established to describe the phenomenon of plasma skimming (Pries et al., 1989; Guibert et al., 2010; Gould and Linninger, 2015; Lee et al., 2016). Among others, the most widely-applied one is probably the Phase-Separation Model (hereafter referred to as PSM) developed by Pries et al. and co-workers based on *in vivo* experiments and theoretical modelling (Pries et al., 1989, 1990, 2003; Pries and Secomb, 2005; Pries, 2019). In brevity, the PSM derived a set of empirical equations from experimental observation of arteriolar bifurcations in rat mesentery, and established a flow-mediated mechanism to quantitatively describe the RBC fluxes received by child branches of diverging bifurcations within a microvascular network.

The PSM correlates the fractional RBC flux FQ_E in a child vessel of a divergent

bifurcation with the fractional blood flow FQ_B that it receives:

$$FQ_E = \frac{1}{1 + \mathrm{e}^{-[A+B\ln(\frac{FQ_B - X_0}{1-(FQ_B+X_0)})]}}, \quad X_0 < FQ_B < 1 - X_0 \tag{1}$$

$$FQ_E = 0, \quad FQ_B \leq X_0 \tag{2}$$

$$FQ_E = 1, \quad FQ_B \geq 1 - X_0 \tag{3}$$

where A, B and X_0 are fitting parameters obtained *via* linear regression analysis. Physically, A reflects the size difference of the two child vessels, B reflects the shape of the haematocrit profile in the parent vessel and X_0 is related to thickness of the cell-depleted layer (or cell-free layer) near the corresponding vessel wall. We follow the formulation of the empirical model in (Pries et al., 2003; Pries and Secomb, 2005):

$$A = -13.29[(D_\alpha^2/D_\beta^2 - 1)/(D_\alpha^2/D_\beta^2 + 1)](1 - H_D)/D_F \tag{4}$$

$$B = 1 + 6.98(1 - H_D)/D_F \tag{5}$$

$$X_0 = 0.964(1 - H_D)/D_F \tag{6}$$

wherein D_α, D_β and D_F are diameters of the two child branches and the parent branch (evaluated in μm), respectively. H_D is the discharge haematocrit of the parent branch.

With D_α, D_β and D_F measured from the ROI geometries and H_D calculated from the simulation data (*via* an RBC-counting procedure), A, B, X_0 can be calculated individually for each bifurcation and the empirical curves are plotted in the form of FQ_E versus FQ_B. Equivalently, the simulation data in the form of Q^*_{rbc} versus Q^*_{blood} are plotted for comparison with the empirical predictions. The results for bifurcations in ROI-1, ROI-2 and ROI-3 are listed in Sec. S2 of the Supplementary Materials (see Figures S1–S3).

6 Acknowledgements

The authors would like to thank Aby Joseph and Jesse Schallek at University of Rochester for providing the *in vivo* data of RBC velocities/fluxes in mouse retina. QZ thanks the University of Edinburgh for the award of a Principal's Career Development Scholarship and an Edinburgh Global Research Scholarship. TP, IF, LTE and HG graciously acknowledge their funding as part of a Foundation Leducq Transatlantic Network of Excellence (17 CVD 03). TK's and MOB's contributions have been funded through two Chancellor's Fellowships at the University of Edinburgh. MOB is supported by grants from EPSRC (EP/R029598/1, EP/R021600/1, EP/T008806/1), Fondation Leducq (17 CVD 03), and the European Union's Horizon 2020 research and innovation programme under grant agreement No 801423. Supercomputing time on the ARCHER UK National Supercomputing Service (http://www.archer.ac.uk) was provided by the "UK Consortium on Mesoscale Engineering Sciences (UKCOMES)" under the EPSRC Grant No. EP/R029598/1. The authors declare that they have no competing financial interests.

References

Aleström, P., D'Angelo, L., Midtlyng, P. J., Schorderet, D. F., Schulte-Merker, S., Sohm, F., and Warner, S. (2019). Zebrafish: Housing and husbandry recommendations. *Laboratory Animals*, page 0023677219869037. Publisher: SAGE Publications.

Amigo, J. D., Ackermann, G. E., Cope, J. J., Yu, M., Cooney, J. D., Ma, D., Langer, N. B., Shafizadeh, E., Shaw, G. C., Horsely, W., Trede, N. S., Davidson, A. J., Barut, B. A., Zhou, Y., Wojiski, S. A., Traver, D., Moran, T. B., Kourkoulis, G., Hsu, K., Kanki, J. P., Shah, D. I., Lin, H. F., Handin, R. I., Cantor, A. B., and Paw, B. H. (2009). The role and regulation of friend of GATA-1 (FOG-1) during blood development in the zebrafish. *Blood*, 114(21):4654–4663. Publisher: American Society of Hematology.

Baeyens, N., Nicoli, S., Coon, B. G., Ross, T. D., Van den Dries, K., Han, J., Lauridsen, H. M., Mejean, C. O., Eichmann, A., Thomas, J.-L., Humphrey, J. D., and Schwartz, M. A. (2015). Vascular remodeling is governed by a VEGFR3-dependent fluid shear stress set point. *eLife*, 4:e04645.

Balogh, P. and Bagchi, P. (2018). Analysis of red blood cell partitioning at bifurcations in simulated microvascular networks. *Physics of Fluids*, 30(5):051902.

Balogh, P. and Bagchi, P. (2019). The cell-free layer in simulated microvascular networks. *Journal of Fluid Mechanics*, 864:768–806.

Bernabeu, M. O., Jones, M. L., Nash, R. W., Pezzarossa, A., Coveney, P. V., Gerhardt, H., and Franco, C. A. (2018). PolNet: A Tool to Quantify Network-Level Cell Polarity and Blood Flow in Vascular Remodeling. *Biophysical Journal*, 114(9):2052–2058.

Bernabeu, M. O., Jones, M. L., Nielsen, J. H., Krüger, T., Nash, R. W., Groen, D., Schmieschek, S., Hetherington, J., Gerhardt, H., Franco, C. A., and Coveney, P. V. (2014). Computer simulations reveal complex distribution of haemodynamic forces in a mouse retina model of angiogenesis. *Journal of The Royal Society Interface*, 11(99):20140543.

Bernabeu, M. O., Köry, J., Grogan, J. A., Markelc, B., Beardo Ricol, A., d'Avezac, M., Kaeppler, J., Daly, N., Hetherington, J., Krüger, T., Maini, P. K., Pitt-Francis, J. M., Muschel, R. J., Alarcón, T., and Byrne, H. M. (2019). Abnormal morphology biases haematocrit distribution in tumour vasculature and contributes to heterogeneity in tissue oxygenation. *bioRxiv*, 640060.

Bhatnagar, P. L., Gross, E. P., and Krook, M. (1954). A Model for Collision Processes in Gases. I. Small Amplitude Processes in Charged and Neutral One-Component Systems. *Physical Review*, 94(3):511–525.

Bouzidi, M., Firdaouss, M., and Lallemand, P. (2001). Momentum transfer of a Boltzmann-lattice fluid with boundaries. *Physics of Fluids*, 13(11):3452–3459.

Boyd, J., Buick, J. M., and Green, S. (2007). Analysis of the Casson and Carreau-Yasuda non-Newtonian blood models in steady and oscillatory flows using the lattice Boltzmann method. *Physics of Fluids*, 19(9):093103.

Bussmann, J., Wolfe, S. A., and Siekmann, A. F. (2011). Arterial-venous network formation during brain vascularization involves hemodynamic regulation of chemokine signaling. *Development*, 138(9):1717–1726.

Carmeliet, P. (2000). Mechanisms of angiogenesis and arteriogenesis. *Nature Medicine*, 6(4):389–395.

Chang, A. H., Raftrey, B. C., D'Amato, G., Surya, V. N., Poduri, A., Chen, H. I., Goldstone, A. B., Woo, J., Fuller, G. G., Dunn, A. R., and Red-Horse, K. (2017). DACH1 stimulates shear stress-guided endothelial cell migration and coronary artery growth through the CXCL12–CXCR4 signaling axis. *Genes & Development*.

Chen, Q., Jiang, L., Li, C., Hu, D., Bu, J.-w., Cai, D., and Du, J.-l. (2012). Haemodynamics-Driven Developmental Pruning of Brain Vasculature in Zebrafish. *PLoS Biol*, 10(8):e1001374.

Clavica, F., Homsy, A., Jeandupeux, L., and Obrist, D. (2016). Red blood cell phase separation in symmetric and asymmetric microchannel networks: effect of capillary dilation and inflow velocity. *Scientific Reports*, 6:srep36763.

Corti, P., Young, S., Chen, C.-Y., Patrick, M. J., Rochon, E. R., Pekkan, K., and Roman, B. L. (2011). Interaction between alk1 and blood flow in the development of arteriovenous malformations. *Development*, 138(8):1573–1582.

Doddaballapur, A., Michalik, K. M., Manavski, Y., Lucas, T., Houtkooper, R. H., You, X., Chen, W., Zeiher, A. M., Potente, M., Dimmeler, S., and Boon, R. A. (2015). Laminar Shear Stress Inhibits Endothelial Cell Metabolism via KLF2-Mediated Repression of PFKFB3Significance. *Arteriosclerosis, Thrombosis, and Vascular Biology*, 35(1):137–145.

Fang, J. S., Coon, B. G., Gillis, N., Chen, Z., Qiu, J., Chittenden, T. W., Burt, J. M., Schwartz, M. A., and Hirschi, K. K. (2017). Shear-induced Notch-Cx37-p27 axis arrests endothelial cell cycle to enable arterial specification. *Nature Communications*, 8(1):2149.

Fenton, B. M., Carr, R. T., and Cokelet, G. R. (1985). Nonuniform red cell distribution in 20 to 100 μm bifurcations. *Microvascular Research*, 29(1):103–126.

Franco, C. A., Blanc, J., Parlakian, A., Blanco, R., Aspalter, I. M., Kazakova, N., Diguet, N., Mylonas, E., Gao-Li, J., Vaahtokari, A., Penard-Lacronique, V., Fruttiger, M., Rosewell, I., Mericskay, M., Gerhardt, H., and Li, Z. (2013). SRF selectively controls tip cell invasive behavior in angiogenesis. *Development*, 140(11):2321–2333.

Franco, C. A., Jones, M. L., Bernabeu, M. O., Geudens, I., Mathivet, T., Rosa, A., Lopes, F. M., Lima, A. P., Ragab, A., Collins, R. T., Phng, L.-K., Coveney, P. V., and Gerhardt, H. (2015). Dynamic Endothelial Cell Rearrangements Drive Developmental Vessel Regression. *PLoS Biol*, 13(4):e1002125.

Franco, C. A., Jones, M. L., Bernabeu, M. O., Vion, A.-C., Barbacena, P., Fan, J., Mathivet, T., Fonseca, C. G., Ragab, A., Yamaguchi, T. P., Coveney, P. V., Lang, R. A., and Gerhardt, H. (2016). Non-canonical Wnt signalling modulates the endothelial shear stress flow sensor in vascular remodelling. *eLife*, 5:e07727.

Freund, J. and Vermot, J. (2014). The Wall-stress Footprint of Blood Cells Flowing in Microvessels. *Biophysical Journal*, 106(3):752–762.

Freund, J. B. (2013). The flow of red blood cells through a narrow spleen-like slit. *Physics of Fluids (1994-present)*, 25(11):110807.

Gould, I. G. and Linninger, A. A. (2015). Hematocrit Distribution and Tissue Oxygenation in Large Microcirculatory Networks. *Microcirculation*, 22(1):1–18.

Guevara-Torres, A., Joseph, A., and Schallek, J. B. (2016). Label free measurement of retinal blood cell flux, velocity, hematocrit and capillary width in the living mouse eye. *Biomedical Optics Express*, 7(10):4228.

Guibert, R., Fonta, C., and Plourabouè, F. (2010). A New Approach to Model Confined Suspensions Flows in Complex Networks: Application to Blood Flow. *Transport in Porous Media*, 83(1):171–194.

Guo, Z., Zheng, C., and Shi, B. (2002). Discrete lattice effects on the forcing term in the lattice Boltzmann method. *Physical Review E*, 65(4):046308.

Hogan, B., Shen, Z., Zhang, H., Misbah, C., and Barakat, A. I. (2019). Shear stress in the microvasculature: influence of red blood cell morphology and endothelial wall undulation. *Biomechanics and Modeling in Mechanobiology*.

Hogan, B. M., Verkade, H., Lieschke, G. J., and Heath, J. K. (2009). Manipulation of Gene Expression During Zebrafish Embryonic Development Using Transient Approaches. In Vincan, E., editor, *Wnt Signaling*, Methods in Molecular Biology, pages 273–300. Humana Press, Totowa, NJ.

Isogai, S., Horiguchi, M., and Weinstein, B. M. (2001). The Vascular Anatomy of the Developing Zebrafish: An Atlas of Embryonic and Early Larval Development. *Developmental Biology*, 230(2):278–301.

Joseph, A., Guevara-Torres, A., and Schallek, J. (2019). Imaging single-cell blood flow in the smallest to largest vessels in the living retina. *eLife*, 8:e45077.

Katanov, D., Gompper, G., and Fedosov, D. A. (2015). Microvascular blood flow resistance: Role of red blood cell migration and dispersion. *Microvascular Research*, 99:57–66.

Kimmel, C. B., Ballard, W. W., Kimmel, S. R., Ullmann, B., and Schilling, T. F. (1995). Stages of embryonic development of the zebrafish. *Developmental Dynamics*, 203(3):253–310.

Kochhan, E., Lenard, A., Ellertsdottir, E., Herwig, L., Affolter, M., Belting, H.-G., and Siekmann, A. F. (2013). Blood Flow Changes Coincide with Cellular Rearrangements during Blood Vessel Pruning in Zebrafish Embryos. *PLOS ONE*, 8(10):e75060.

Krogh, A. (1921). Studies on the physiology of capillaries. *The Journal of Physiology*, 55(5-6):412–422.

Krüger, T. (2012). *Computer Simulation Study of Collective Phenomena in Dense Suspensions of Red Blood Cells under Shear*. Vieweg+Teubner Verlag.

Krüger, T., Varnik, F., and Raabe, D. (2011). Efficient and accurate simulations of deformable particles immersed in a fluid using a combined immersed boundary lattice Boltzmann finite element method. *Computers & Mathematics with Applications*, 61(12):3485–3505.

Ladd, A. J. C. (1994). Numerical simulations of particulate suspensions via a discretized Boltzmann equation. Part 1. Theoretical foundation. *Journal of Fluid Mechanics*, 271:285–309.

Lanotte, L., Mauer, J., Mendez, S., Fedosov, D. A., Fromental, J.-M., Claveria, V., Nicoud, F., Gompper, G., and Abkarian, M. (2016). Red cells' dynamic morphologies govern blood shear thinning under microcirculatory flow conditions. *Proceedings of the National Academy of Sciences*, page 201608074.

Lee, T.-R., Yoo, S. S., and Yang, J. (2016). Generalized plasma skimming model for cells and drug carriers in the microvasculature. *Biomechanics and Modeling in Mechanobiology*, pages 1–11.

Li, Y.-S. J., Haga, J. H., and Chien, S. (2005). Molecular basis of the effects of shear stress on vascular endothelial cells. *Journal of Biomechanics*, 38(10):1949–1971.

Lim, G. H. W., Wortis, M., and Mukhopadhyay, R. (2009). Red Blood Cell Shapes and Shape Transformations: Newtonian Mechanics of a Composite Membrane: Sections 2.1–2.4. In *Soft Matter*, pages 83–139. John Wiley & Sons, Ltd.

Lu, H. and Peng, Z. (2019). Boundary integral simulations of a red blood cell squeezing through a submicron slit under prescribed inlet and outlet pressures. *Physics of Fluids*, 31(3):031902.

Lucitti, J. L., Jones, E. A. V., Huang, C., Chen, J., Fraser, S. E., and Dickinson, M. E. (2007). Vascular remodeling of the mouse yolk sac requires hemodynamic force. *Development*, 134(18):3317–3326.

Mack, J. J., Mosqueiro, T. S., Archer, B. J., Jones, W. M., Sunshine, H., Faas, G. C., Briot, A., Aragón, R. L., Su, T., Romay, M. C., McDonald, A. I., Kuo, C.-H., Lizama, C. O., Lane, T. F., Zovein, A. C., Fang, Y., Tarling, E. J., de Aguiar Vallim, T. Q., Navab, M., Fogelman, A. M., Bouchard, L. S., and Iruela-Arispe, M. L. (2017). NOTCH1 is a mechanosensor in adult arteries. *Nature Communications*, 8(1):1620.

Neal, A., Nornes, S., Payne, S., Wallace, M. D., Fritzsche, M., Louphrasitthiphol, P., Wilkinson, R. N., Chouliaras, K. M., Liu, K., Plant, K., Sholapurkar, R., Ratnayaka, I., Herzog, W., Bond, G., Chico, T., Bou-Gharios, G., and Val, S. D. (2019). Venous identity requires BMP signalling through ALK3. *Nature Communications*, 10(1):453.

Noble, F. l., Moyon, D., Pardanaud, L., Yuan, L., Djonov, V., Matthijsen, R., Bréant, C., Fleury, V., and Eichmann, A. (2004). Flow regulates arterial-venous differentiation in the chick embryo yolk sac. *Development*, 131(2):361–375.

Obrist, D., Weber, B., Buck, A., and Jenny, P. (2010). Red blood cell distribution in simplified capillary networks. *Philosophical Transactions of the Royal Society A: Mathematical, Physical and Engineering Sciences*, 368(1921):2897–2918.

Oulaid, O. and Zhang, J. (2015). Temporal and Spatial Variations of Wall Shear Stress in the Entrance Region of Microvessels. *Journal of Biomechanical Engineering*, 137(6):061008.

Peskin, C. S. (2002). The immersed boundary method. *Acta Numerica*, 11:479–517.

Potente, M., Gerhardt, H., and Carmeliet, P. (2011). Basic and Therapeutic Aspects of Angiogenesis. *Cell*, 146(6):873–887.

Pries, A. R. (2019). Microvascular hemodynamics: System properties. *Biorheology*, Preprint(Preprint):1–13.

Pries, A. R., Ley, K., Claassen, M., and Gaehtgens, P. (1989). Red cell distribution at microvascular bifurcations. *Microvascular Research*, 38(1):81–101.

Pries, A. R., Reglin, B., and Secomb, T. W. (2003). Structural response of microcirculatory networks to changes in demand: information transfer by shear stress. *American Journal of Physiology - Heart and Circulatory Physiology*, 284(6):H2204–H2212.

Pries, A. R. and Secomb, T. W. (2005). Microvascular blood viscosity in vivo and the endothelial surface layer. *American Journal of Physiology - Heart and Circulatory Physiology*, 289(6):H2657–H2664.

Pries, A. R. and Secomb, T. W. (2008). Chapter 1 - Blood Flow in Microvascular Networks. In Tuma, R. F., Durán, W. N., and Ley, K., editors, *Microcirculation (Second Edition)*, pages 3–36. Academic Press, San Diego.

Pries, A. R., Secomb, T. W., Gaehtgens, P., and Gross, J. F. (1990). Blood flow in microvascular networks. Experiments and simulation. *Circulation Research*, 67(4):826–834.

Pries, A. R., Secomb, T. W., Gessner, T., Sperandio, M. B., Gross, J. F., and Gaehtgens, P. (1994). Resistance to blood flow in microvessels in vivo. *Circulation Research*, 75(5):904–915.

Pries, A. R., Secomb, T. W., Jacobs, H., Sperandio, M., Osterloh, K., and Gaehtgens, P. (1997). Microvascular blood flow resistance: role of endothelial surface layer. *American Journal of Physiology - Heart and Circulatory Physiology*, 273(5):H2272–H2279.

Qian, Y. H., D'Humières, D., and Lallemand, P. (1992). Lattice BGK Models for Navier-Stokes Equation. *EPL (Europhysics Letters)*, 17(6):479.

Salehyar, S. and Zhu, Q. (2016). Deformation and internal stress in a red blood cell as it is driven through a slit by an incoming flow. *Soft Matter*, 12(13):3156–3164.

Salehyar, S. and Zhu, Q. (2017). Effects of stiffness and volume on the transit time of an erythrocyte through a slit. *Biomechanics and Modeling in Mechanobiology*, 16(3):921–931.

Shen, Z., Coupier, G., Kaoui, B., Polack, B., Harting, J., Misbah, C., and Podgorski, T. (2016). Inversion of hematocrit partition at microfluidic bifurcations. *Microvascular Research*, 105:40–46.

Sherwood, J. M., Holmes, D., Kaliviotis, E., and Balabani, S. (2014). Spatial Distributions of Red Blood Cells Significantly Alter Local Haemodynamics. *PLOS ONE*, 9(6):e100473.

Stapor, P. C., Bock, P. K. D., and Carmeliet, P. P. (2014). Essentials of Angiogenesis. In Lanzer, P., editor, *PanVascular Medicine*, pages 1–34. Springer Berlin Heidelberg.

Tomaiuolo, G. (2014). Biomechanical properties of red blood cells in health and disease towards microfluidics. *Biomicrofluidics*, 8(5):051501.

Vion, A.-C., Alt, S., Klaus-Bergmann, A., Szymborska, A., Zheng, T., Perovic, T., Hammoutene, A., Oliveira, M. B., Bartels-Klein, E., Hollfinger, I., Rautou, P.-E., Bernabeu, M. O., and Gerhardt, H. (2018). Primary cilia sensitize endothelial cells to BMP and prevent excessive vascular regression. *J Cell Biol*, 217(5):1651–1665.

Yashiro, K., Shiratori, H., and Hamada, H. (2007). Haemodynamics determined by a genetic programme govern asymmetric development of the aortic arch. *Nature*, 450(7167):285–288.

Supplementary materials

S1 Simulations of cellular blood flow in microvascular networks of mouse retina

The immersed-boundary-lattice-Boltzmann method (IB-LBM; Krüger, 2012) is employed to model blood flow as a suspension of deformable RBCs. The fluid flow governed by the Navier-Stokes equations is solved by the lattice-Boltzmann method (LBM) with standard D3Q19 lattice (Qian et al., 1992), BGK collision operator (Bhatnagar et al., 1954) and Guo's forcing scheme (Guo et al., 2002). The no-slip condition on vessel walls is implemented with the Bouzidi-Firdaouss-Lallemand method (BFL; Bouzidi et al., 2001). Open boundaries are handled with the Ladd implementation of velocity boundary conditions (Ladd, 1994) for control of volume flow rates at multiple inlets and outlets. The RBCs are modelled as Lagrangian membranes using a finite element method (FEM). The fluid structure interaction (FSI) between the flow and the RBC membranes is realised using the immersed-boundary method (IBM; Peskin, 2002), which tackles the velocity interpolation and force spreading. The algorithm coupling the LBM, FEM and IBM is implemented in the open-source blood flow simulation software *HemeLB* (Bernabeu et al., 2014; `http://ccs.chem.ucl.ac.uk/hemelb`) for parallel computing.

Each RBC is modelled as a closed membrane consisting of N_f triangular facets and present a discocyte shape at rest (Krüger, 2012). The mesh resolution of the membrane (namely N_f) matches the lattice size Δx of the flow domain for numerical stability and accuracy (see Krüger et al., 2011 for a detailed numerical analysis). The RBC membrane is hyperelastic, isotropic and homogeneous. Its mechanical properties are controlled by several moduli (κ_s, κ_b, κ_α, κ_A, κ_V) governing energy contributions from strain, bending, area and volume of the membrane (see Table S1). Enclosed by the RBC membrane is the cytosol treated as a Newtonian fluid of plasma viscosity. The viscosity of the RBC membrane itself is not considered in the present material model.

The morphological deformation of an RBC in small vessels or channels are known to be dominated by the strain modulus κ_s and the bending modulus κ_b, both of which have been extensively measured for healthy human RBCs using diverse experimental techniques. The commonly accepted values from different experiments are $\kappa_s = 5.5 \pm 3.3\,\mu$N/m and $\kappa_b = 1.15 \pm 0.9 \times 10^{-19}$ Nm, respectively (see reviews (Lim et al., 2009) and (Tomaiuolo, 2014)). However, because these measurements all rely on certain deformation protocols that do not necessarily reflect the complex microcirculatory conditions, the obtained values may not apply to RBCs travelling in capillary networks of the mouse retina. Indeed, we find that the κ_s and κ_b required to maintain the integrity of the RBC membrane in our cellular simulations are roughly one order larger in magnitude than the reported values (see the simulation values in Table S1). This substantial increase in required κ_s and κ_b for reasonable RBC morphology may also arise from the intrinsic difference in the haemodynamic environment (*e.g.* magnitude ranges of the shear rate and wall shear stress) of the microcirculation system between mice and humans.

Table S1: Key parameters of the RBC model. The symbol "$\sim$" represents dimensionless simulation units. Please refer to (Krüger, 2012) for more details of the RBC model.

Parameter	Description	Value	Unit	Comment or reference
r_{rbc}	RBC radius	4	μm	(Lim et al., 2009)
A_{rbc}	RBC surface	140	μm^2	(Lim et al., 2009)
V_{rbc}	RBC volume	100	μm^3	(Lim et al., 2009)
η_{plasma}	plasma viscosity	1	mPa s	modelled as liquid water
$\eta_{cytosol}$	artificial cytosol viscosity	1	mPa s	assuming $\eta_{cytosol} = \eta_{plasma}$
$\Gamma_{nominal}$	Föppl-von Kármán number	400	–	$\Gamma_{nominal} = \frac{\kappa_s r_{rbc}^2}{\kappa_b}$
N_f	number of facets	1280	–	$N_f = 20(\frac{r_{rbc}}{\Delta x})^2$
κ_s	strain modulus	50	μN/m	resisting in-plane shearing
κ_b	bending modulus	2×10^{-18}	Nm	resisting off-plane bending
$\tilde{\kappa}_\alpha$	dilation modulus	0.5	–	conserving local area
$\tilde{\kappa}_A$	surface modulus	1	–	conserving RBC surface
$\tilde{\kappa}_V$	volume modulus	1	–	conserving RBC volume

S2 Evaluation of simulation data against empirical model

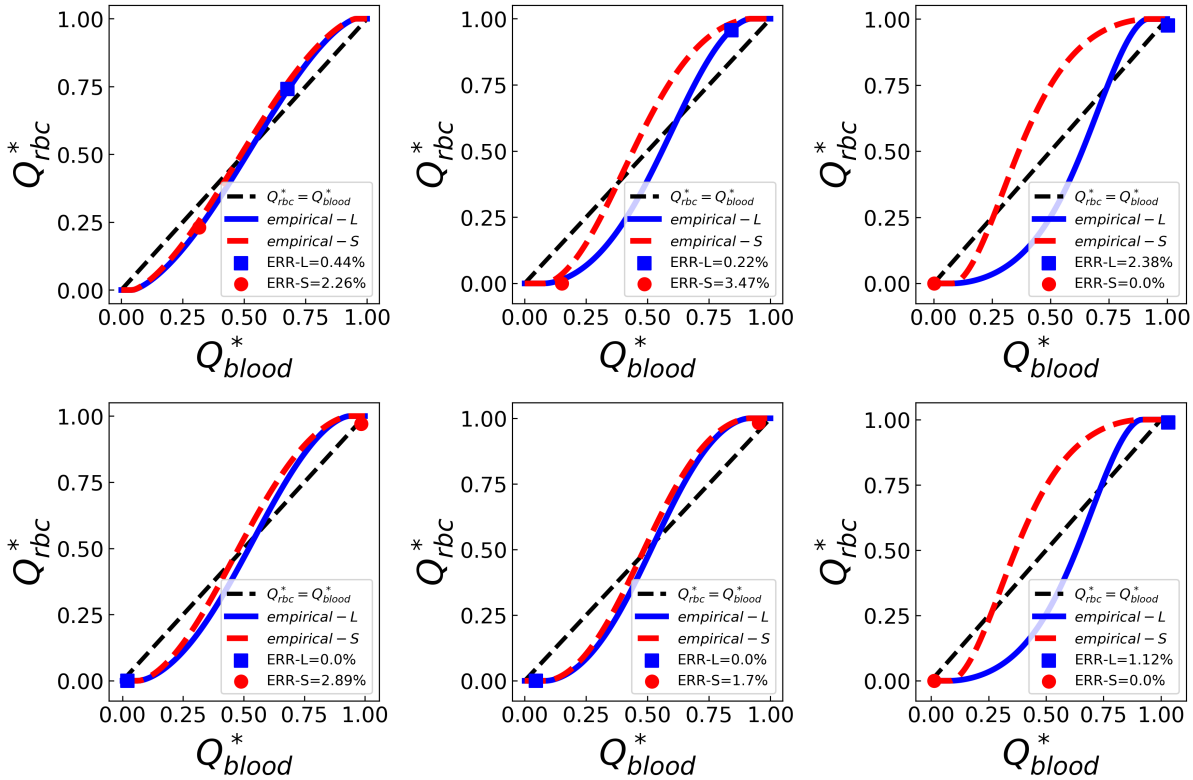

Figure S1: Evaluation of simulation data against the empirical predictions represented as fractional RBC flux Q^*_{rbc} against fractional blood flow Q^*_{blood} for all divergent bifurcations identified in ROI-1 (see Figure 8a). The simulation data are represented by squares/circles and the empirical predictions by solid lines. In each bifurcation, the relatively larger child branch is termed "L" and relatively smaller child branch termed "S". The black dashed line represent a linear hypothesis for Q^*_{rbc} and Q^*_{blood} in the absence of plasma skimming.

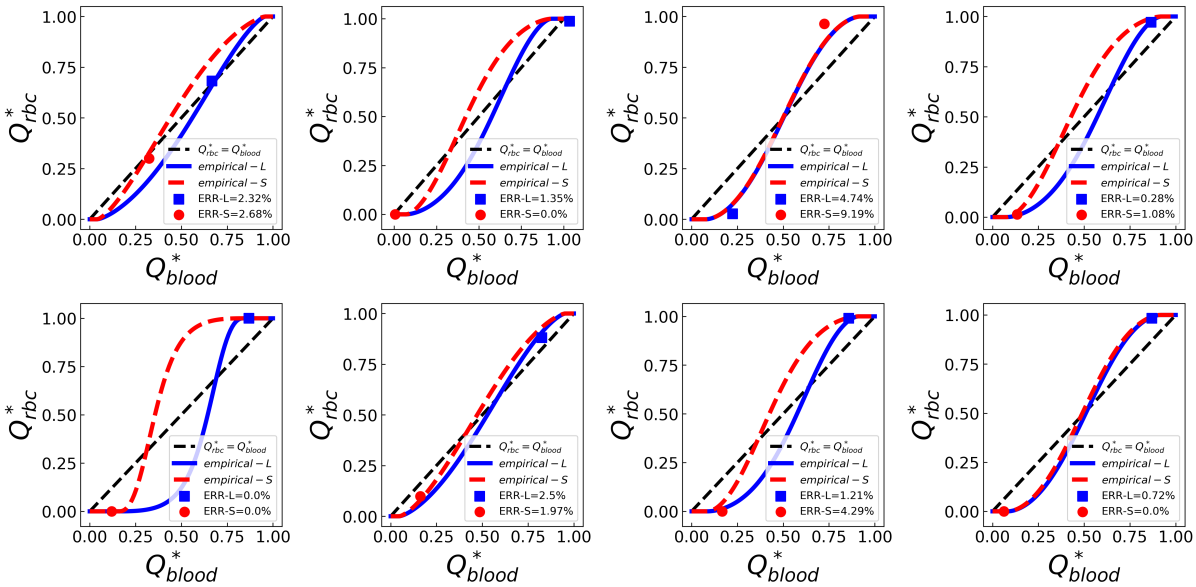

Figure S2: Evaluation of simulation data against the empirical predictions represented as fractional RBC flux Q^*_{rbc} against fractional blood flow Q^*_{blood} for all divergent bifurcations identified in ROI-2 (see Figure 8b). The simulation data are represented by squares/circles and the empirical predictions by solid lines. In each bifurcation, the relatively larger child branch is termed "L" and relatively smaller child branch termed "S". The black dashed line represent a linear hypothesis for Q^*_{rbc} and Q^*_{blood} in the absence of plasma skimming.

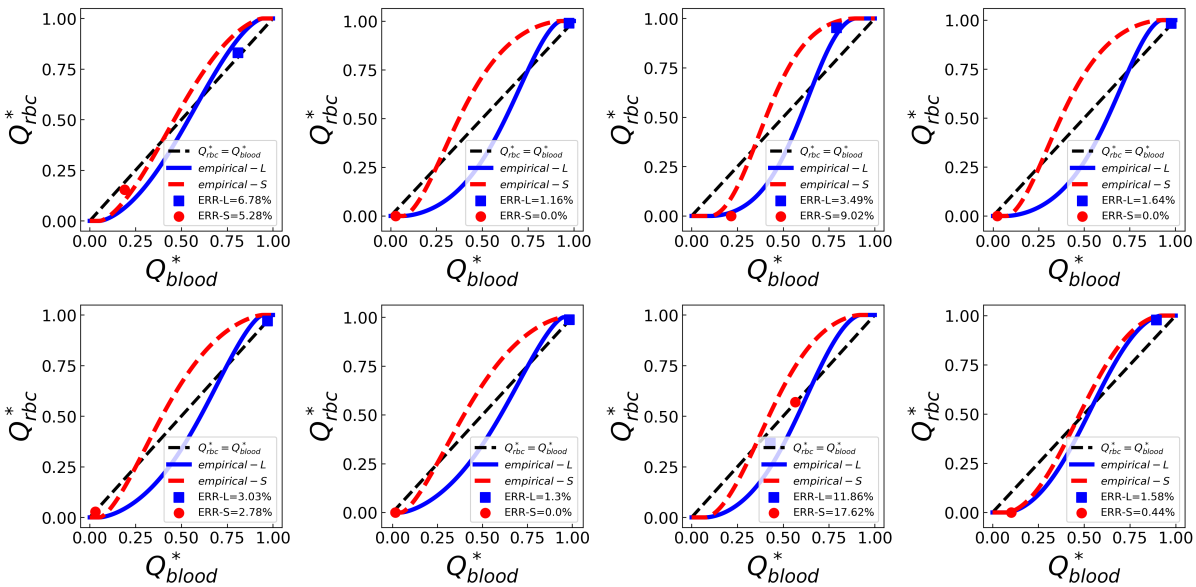

Figure S3: Evaluation of simulation data against the empirical predictions represented as fractional RBC flux Q^*_{rbc} against fractional blood flow Q^*_{blood} for all divergent bifurcations identified in ROI-3 (see Figure 8c). The simulation data are represented by squares/circles and the empirical predictions by solid lines. In each bifurcation, the relatively larger child branch is termed "L" and relatively smaller child branch termed "S". The black dashed line represent a linear hypothesis for Q^*_{rbc} and Q^*_{blood} in the absence of plasma skimming.

S3 Asymmetry of velocity profile in RBC flow

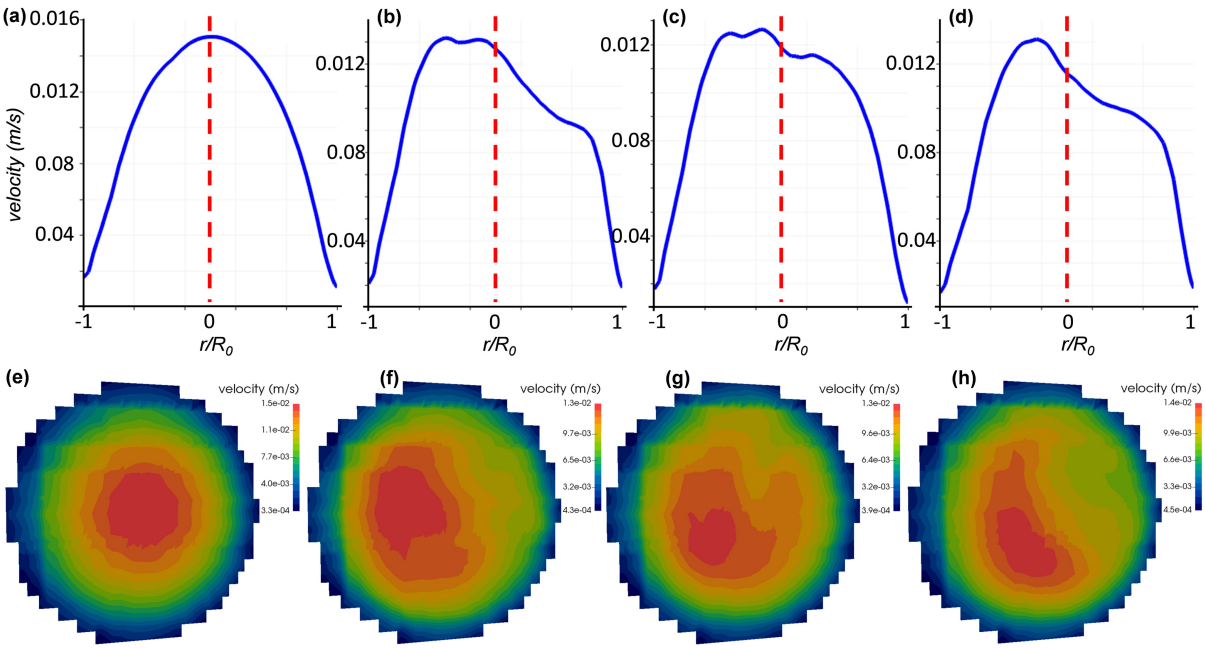

Figure S4: (a-d) Velocity profiles over time at the red solid line labelled in Figure 4d. (e-h) Corresponding cross-sectional velocity contours at the same position. (a) and (e): $t_1 = 0.042$s. (b) and (f): $t_2 = 0.125$s. (c) and (g): $t_3 = 0.208$s. (d) and (h): $t_4 = 0.291$s.